Natural Hazards
https://doi.org/10.1007/s11069-020-04180-9

ORIGINAL PAPER

Zoning map for drought prediction using integrated machine learning models with a nomadic people optimization algorithm

Sedigheh Mohamadi[1] · **Saad Sh. Sammen**[2] · **Fatemeh Panahi**[3] · **Mohammad Ehteram**[4] · **Ozgur Kisi**[5,6] · **Amir Mosavi**[7,8] · **Ali Najah Ahmed**[9] · **Ahmed El-Shafie**[10,11] · **Nadhir Al-Ansari**[12]

Received: 12 May 2020 / Accepted: 10 July 2020

Abstract

The modelling of drought is of utmost importance for the efficient management of water resources. This article used the adaptive neuro-fuzzy interface system (ANFIS), multilayer perceptron (MLP), radial basis function neural network (RBFNN), and support vector machine (SVM) models to forecast meteorological droughts in Iran. The spatial–temporal pattern of droughts in Iran was also found using recorded observation data from 1980 to 2014. A nomadic people algorithm (NPA) was utilized to train the ANFIS, MLP, RBFNN, and SVM models. Additionally, the NPA was benchmarked against the bat algorithm, salp swarm algorithm, and krill algorithm (KA). The hybrid ANFIS, MLP, RBFNN, and SVM models were used to forecast the 3-month standardized precipitation index. New evolutionary algorithms were utilized to improve the convergence speed of the soft computing models and their accuracy. First, random stations, namely, in Azarbayjan (northwest Iran), Khouzestan (southwest Iran), Khorasan (northeast Iran), and Sistan and Balouchestan (southeast Iran) were selected for the testing of the models. According to the results obtained from the Azarbayjan station, the Nash–Sutcliffe efficiency (NSE) was 0.93, 0.86, 0.85, and 0.83 for the ANFIS–NPA, MLP–NPA, RBFNN–NPA, and SVM–NPA models, respectively. For Sistan and Baloucehstan, the results indicated the superiority of the ANFIS–NPA model, followed by the MLP–NPA model, compared to the RBFNN–NPA and SVM–NPA models, and suggested that the hybrid models performed better than the standalone MLP, RBFNN, ANFIS, and SVM models. The second aim of the study was to capture the relationship between large-scale climate signals and drought indices by using a wavelet coherence analysis. The general results indicated that the NPA and wavelet coherence analysis are useful tools for modelling drought indices.

Keywords Drought · SPI · ANFIS · MLP · SVM · Nomadic people optimization algorithm

---

✉ Saad Sh. Sammen
saad123engineer@yahoo.com

Amir Mosavi
amirhosein.mosavi@tdtu.edu.vn

Extended author information available on the last page of the article

1 Introduction

Rainfall deficiency can lead to drought, which is a creeping natural hazard. Drought leads to tremendous losses to the ecosystem and agriculture. The climatological community has categorized drought events into four types: meteorological, hydrological, agricultural, and socioeconomic (Kaur and Sood 2019). When dry weather patterns dominate in a region, a meteorological drought occurs. Agricultural droughts connect various features of meteorological droughts to agricultural impacts, concentrating on the shortage of soil moisture and reduced groundwater level (Liu et al. 2020). Hydrological droughts take place when there is a deficiency in precipitation (Rahimi et al. 2019). A socioeconomic drought occurs when people are physically affected by a water deficiency. Meteorological droughts are defined by temporal rainfall variations in each station. Rainfall shortages are known to be indicators of meteorological droughts (Mokhtarzad et al. 2017; Shamshirband et al. 2020). Many parameters, such as soil moisture and surface flow generation, have a significant impact on rainfall shortage. Meteorological droughts result from a decreasing trend of rainfall in a region (Mokhtarzad et al. 2017). Meteorological drought indices are provided by converting meteorological droughts into numerical values (Huang et al. 2016). Hydrological droughts are very significant for agricultural activities and urban areas. Agricultural droughts are affected by hydrological droughts (Le et al. 2016). Agricultural droughts are described by defining soil water and moisture (Hao et al. 2018). A socioeconomic drought results from a weather-related shortfall in the water supply. Demand patterns and water supply have significant effects on socioeconomic droughts (Shi et al. 2018). Challenges still exist in drought predictions. The first challenge is identifying the relationship between droughts and meteorological parameters. The second challenge is the selection of accurate models for predicting droughts. In recent years, different studies have attempted to use different methods for finding the relationship between large-scale climate signals, such as the Arctic Oscillation (AO) Index, the Southern Oscillation Index (SOI), the North Atlantic Oscillation (NAO) Index, Niño 3.4, the Pacific mean sea surface temperature (SST), and drought indices (DI) (Saghafian et al. 2017). There are different methods of finding the link between large-scale climate signals and drought indices. The wavelet coherence method is widely used for finding the relationship between climate patterns and hydrological variables such as drought, rainfall, and streamflow. Su et al. (2019) used the wavelet coherence transform to identify temporal patterns in streamflow. Das et al. (2020) used wavelet coherence approaches to study the effects of large-scale climate signals on monthly precipitations over different regions in India. The results indicated that the wavelet coherence method is powerful in analysing the relationship between large-scale climate signals and monthly precipitations. Li et al. (2020a) used a cross-wavelet analysis to examine the propagation of agricultural drought. The modelling results indicated that the propagation of agricultural droughts was 2–3 months from a hydrological to vegetation drought. Li et al. (2020b) used a wavelet analysis to identify the periodic relationship between hydrological and meteorological droughts. The results revealed that meteorological and hydrological droughts show similar patterns in terms of phase shifts.

Drought indices are of significant importance in forecasts and characterizations. While remote sensing, spatial modelling, and geographic data are used to forecast droughts, these technologies are not well-combined with multilevel social co-operative responses (Le et al. 2016). Recently, soft computing models such as artificial neural networks (ANNs), adaptive neuro-fuzzy interface system (ANFIS) models, genetic programming, support vector machines (SVMs), and the tree decision model have been utilized for predicting droughts

(Deo et al. 2018). ANN models use a large set of elementary computational units to model complex events. Unseen relationships on unseen data are well inferred by ANN models. The unexplained behaviour of ANN models is one of their major disadvantages (Deo et al. 2018). ANN models generate the relationship between variables without being instructed.

In this context, Barua et al. (2010) applied the ANN model for drought forecasting. Their study compared two kinds of ANNs, namely, the direct multistep neural network (DMSNN) and the recursive multistep neural network (RMSNN). Their findings indicated that the RMSNN slightly outperformed the DMSNN model. Rezaeian-Zadeh and Tabari (2012) used a multilayer perceptron model for predicting droughts. In their study, different input combinations were used to predict the standardized precipitation index (SPI). Borji et al. (2016) used the ANN and SVM models to forecast the streamflow drought index (SDI). A gamma test was used to identify the appropriate input combinations. The results indicated that the SVM model outperformed the ANN in forecasting long-term droughts. Belayneh et al. (2016) explored the ability of the wavelet ANN and wavelet SVM to forecast droughts in Ethiopia. The results revealed that the wavelet ANN and wavelet SVM performed better than the ANN and SVM models.

Mokhtarzad et al. (2017) used the ANN, ANFIS, and SVM to model the SPI. They reported that the SVM model showed a high level of accuracy compared to the ANFIS and ANN models. Hosseini-Moghari et al. (2017) used a recursive multilayer perceptron (RMLP) and SVM to model droughts. They used the imperialist competitive algorithm (ICA) to optimize the performance of the SVM and RMLP models.

The SVM model is important for hydrological variables. SVM models are effective in high-dimensional spaces. The main disadvantage of SVMs is that they have several important parameters that need to be correctly adjusted to obtain the best results for any given problem (Mokhtarzd et al. 2017). The identification of a kernel function requires previous experience to obtain the best results for different case studies.

In this context, Deo et al. (2017) used the least squares support vector machine (LSSVM) and M5Tree for the modelling of the SPI. Their findings indicated that the M5Tree model was better than the LLSVM model. Zhang et al. (2019) compared the predicting abilities of the wavelet neural network (WNN), the autoregressive integrated moving average (AIRMA), and the SVM for the prediction of droughts in China. Their findings revealed that the AIRMA model showed an obvious advantage over the SVM and WNN models. Rahmati et al. (2020) developed the SVM, random forest (RF), and classification regression trees for the spatial modelling of agricultural droughts. A quantitative analysis indicated that the use of soft computing models was able to construct a risk map for the study area. Shamshirband et al. (2020) used an SVM, M5 model tree (M5T), and gene express programming (GEP) to predict the standardized precipitation index.

Recently, ANFIS models have been widely implemented for the modelling of hydrological variables. Neguyan et al. (2017) utilized an ANFIS model for drought prediction. The sea surface temperatures (SSTs) at Nino4 zones were chosen as the input variables.

Kisi et al. (2019) used the ANFIS genetic algorithm (GA), ANFIS particle swarm optimization (PSO), ANFIS firefly algorithm (FFA), and ANFIS butterfly optimization algorithm (BOA) for modelling droughts. It was observed that the evolutionary ANFIS models performed better than the standalone ANFIS model. Malik et al. (2019) utilized the coactive neuro-fuzzy interface system (CANFIS), multilayer perceptron (MLP) model, and multiple linear regression (MLR) model to forecast hydrological droughts.

Model inputs are structured on a complexity of drought forecasts. Drought indices are forecast on different time scales. Literature reviews predicted droughts on the basis of drought indices with different lead times. A number of studies have used the gamma test for capturing optimal input combinations. Borji et al. (2016) used the gamma test to predict values for a 9-month, 12-month, and 24-month streamflow drought index. The optimization of soft computing parameters is another challenge for modelers.

Recently, soft computing models have been trained by optimization algorithms (Moazenzadeh et al. 2018). These new optimization algorithms can improve the accuracy and the convergence speed of soft computing models for predicting hydrological variables. The nomadic people algorithm (NPA) is a new optimization algorithm that was introduced by Salih and Alsewari (2019). The algorithm was successfully tested for large-scale optimization problems and benchmark functions. The NPA was inspired by the behaviour of nomadic people. The NPA can find optimal solutions in a rapid manner because of the meeting room operator. The NPA uses the meeting room operator to share information between the best solutions and other solutions. The advantages of the NPA are its ability to find global solutions and its fast convergence speed.

In this regard, the first aim of this study was to design new hybrid ANFIS, ANN, and SVM models for predicting droughts. The ANN, ANFIS, and SVM models were trained by the NPA to forecast droughts. However, the ANFIS, SVM and ANN models should be improved in different aspects such as in terms of accuracy and convergence speed (Alighorbani et al. 2018; Wu and Chau 2013). The NPA was benchmarked against other optimization algorithms, namely, the bat algorithm (BA), salp swarm algorithm (SSA), and krill algorithm (KA). The new algorithms were benchmarked against the NPA because of its ability to solve different global optimization problems. These algorithms have different operators so that each operator changes the accuracy of the obtained results (Wang et al. 2020). The second aim of the current study was to use the wavelet coherence method to detect the relationship between large-scale climate signals and drought indices. Although there are different methods for finding a relationship between climate parameters and target variables, the wavelet coherence can present the results accurately and in greater detail.

The novelty of the current paper is related to the hybridization of new optimization algorithms and soft computing models. The new hybrid soft computing models can be used for predicting other hydrological variables.

First, soft computing models were used to forecast drought indices. Next, the wavelet coherence approach was used to investigate the effects of large-scale climate signals on drought indices.

2 Materials and methods

2.1 Adaptive neuro-fuzzy interface system (ANFIS)

The ANFIS model can simulate nonlinearity functions, and simulate the features of a dataset. It uses human knowledge to construct input–output mapping (Mokhtarzad et al. 2017; Gholami et al. 2019; Cheng et al. 2005). The ANFIS model acts on the basis of the Sugeno fuzzy interface system suggested by Takagi and Sugeno. Figure 1 shows a fuzzy system.

The ANFIS model has a five-layer structure.

Layer 1: The outputs of the first layer are the degrees of membership functions.

$$\begin{aligned} O_{1,i} &= \mu A_{i(x)} \\ O_{1,i} &= \mu B_{i-2(y)} \end{aligned} \tag{1}$$

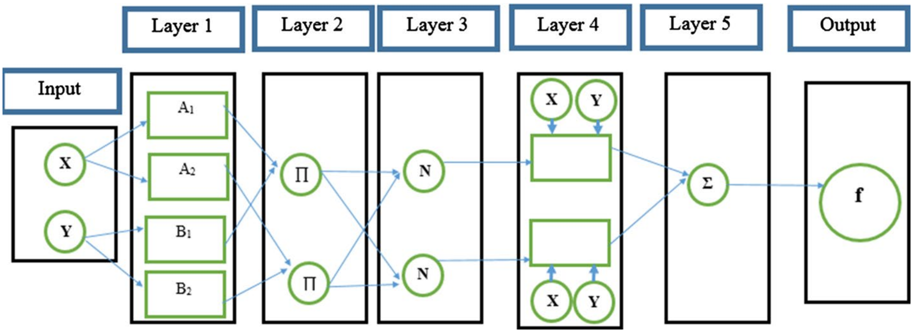

Fig. 1 The structure of the ANFIS model

where $\mu A_{i(x)}$ and $O_{1,i} = \mu B_{i-2(y)}$: the degrees of membership of fuzzy function sets of A_i and B_i, and $O_{1,i}$: the output of the first layer.

Layer 2: This includes the fixed nodes. The signal input and output are computed by each node. All the nodes in this layer are labelled with a Π:

$$O_{2,i} = \omega = \mu A_i(y)B(y). \tag{2}$$

ω: the fuzzy strength of each rule.

Layer 3: All the nodes are labelled as N. The nodes of this layer play the role of normalization in the network:

$$O_{3,i} = \overline{\omega}_i = \frac{\omega_i}{\sum_{j=1}^{2} \omega_j} \tag{3}$$

where $O_{3,i}$: the output of the third layer.

Layer 4: The output is the product of the normalized firing strength and a first-order polynomial:

$$O_{4,i} = \overline{\omega}_i f_i = \overline{\omega}\left(p_i x + q_i y + r_i\right) \tag{4}$$

where p, q, r: consequent parameters.

Layer 5: The input signal sum is computed as follows:

$$O_{5,i} = \sum_i \overline{\omega}_i f_i = \frac{\sum_i \omega_i f_1}{\sum_i \omega_i} \tag{5}$$

The Bell membership functions are widely used for the ANFIS model due to their smoothness and concise notation,

$$\mu_x(a) = \frac{1}{1 + \left(\frac{a-z}{x}\right),} \tag{6}$$

where a and z are the premise parameters. The classical ANFIS model uses the recursive least squares method to find the optimal values of the consequent parameters. The ANFIS model uses the backpropagation algorithm to find the premise parameters. However, the classical training algorithms may get trapped in local optima (Khosravi et al. 2017). Thus,

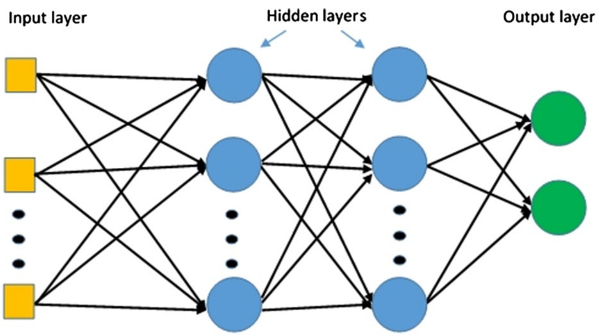

Fig. 2 The schematic of structure of MLP model

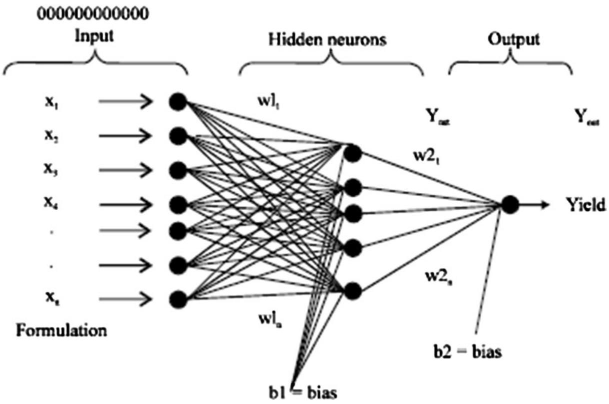

Fig. 3 The Structure of RBFNN model (Tortoe et al. 2011)

it is necessary to use robust optimization algorithms as alternative algorithms. Optimization algorithms have a high convergence rate and flexibility (Fig. 1). The key parameters of the ANFIS model were obtained by the optimization algorithms.

2.2 Multilayer perceptron (MLP)

MLP models are famous forms of ANN models. MLP models are composed of a number of neurons that act as processing units distributed over a series of fully-linked layers. Data transition in the MLP happens between three layers (Ghorbani et al. 2018). The connections between the different layers are identified by weights (Fig. 2).

To approximate the output, different learning algorithms are used to train the ANN models The backpropagation algorithm is broadly applied to train ANN models. The main drawback of backpropagation is that it can be sensitive to noisy data (Fig. 2). The optimization algorithms obtained the key parameters of the MLP.

2.3 Radial basis function neural network (RBFNN)

The RBFNN is commonly applied for the prediction of hydrological variables. Figure 3 indicates the structure of the RBNN model. First, each hidden neuron receives an input vector, and each hidden node independently calculates an intermediate output variable (Zhao et al. 2019). Second, the intermediate hidden node output values are integrated to provide the output values. The output of the hidden node is computed as follows:

$$\phi_j = e^{-\frac{\left\|x-\mu_j\right\|}{2\sigma_j^2}} \tag{7}$$

where ϕ_j is a Gaussian function; σ is the width of the hidden neuron, i; and μ is the centre of the hidden neuron. The outputs of the RBFNN are computed as follows:

$$y_i = \sum_{j=1}^{n} \omega_{ji}\phi_j(x) \tag{8}$$

where ω_{ji} is the ith weight between the hidden and output layers; and n is the number of hidden nodes. Classical training algorithms are commonly used to find the optimal values of the width and the centre of the hidden neuron, as follows:

$$\begin{aligned} &\hat{y} = \left(y_1, y_2, \ldots, y_m\right) = \begin{bmatrix} \omega_{11} & & \omega_{1m} \\ . & . & . \\ \omega_{I1} & . & \omega_{\mathrm{Im}} \end{bmatrix} \\ &O = W \cdot H \end{aligned} \tag{9}$$

$$\begin{aligned} &E = \frac{1}{2}\sum_{k=1}^{M}\sum_{i=1}^{L}\left(y_{i,k} - \hat{y}_{i,k}\right)^2 \\ &\omega_{ij} = \omega_{ij} - \eta\frac{\partial E}{\partial \omega} \end{aligned} \tag{10}$$

where E is the error function; $y_{i,k}$ is the observed value; $\hat{y}_{i,k}$ is the estimated value; η is the learning rate; L is the number of output neurons; and M is the number of hidden neurons. The gradient descent method has slow convergence. Thus, the RBFNN models were trained by evolutionary algorithms (Fig. 3).

2.4 SVM model

The SVM model is widely applied to regression analysis, hydrological simulation, and clustering analysis. The main equation of the SVM model is as follows (Bui et al. 2017):

$$f(x) = w^{\mathrm{Tr}} \cdot x + b \tag{11}$$

where x is the input; w is the weight vector of the input variable; b is the bias value; and Tr is the transpose sign. An error of function is utilized to avoid the over-fitting deficit:

$$|y - f(x)| = \begin{bmatrix} 0 \\ |y - f(x)| - \psi = \xi \end{bmatrix}, \tag{12}$$

where y is the observed value; ψ is the error threshold; and ξ is the penalty for prediction errors that are outside of the range $(-\psi, +\psi)$. The following equation was minimized by the SVM model:

$$\begin{aligned} \text{Minimize} \quad & \frac{1}{2}\|w\|^2 + C\sum_{i=1}^{m}\left(\xi_i^- + \xi_i^+\right) \\ \text{subject(to)} \quad & \left(w_i.x_i + b\right) - y_i < \psi + \xi_i^+ \\ & y_i - \left(w_i.x_i + b\right) \le \psi + \xi_i^-, \end{aligned} \tag{13}$$

where C is the penalty function; m is the training data number; ξ_i^- and ξ_i^+ are the violations of the ith training point; x_i is the input variable; y is the output variable; and w is the weight. Equation (17) was used to compute the values of w and b. The kernel functions were used to map the dataset to the linear separable space. Thus, Eq. (14) could be rewritten as follows:

$$f(x) = w^{Tr} \cdot K\left(x, x_i\right) + b \tag{14}$$

$$K\left(x, x_i\right) = \exp\left(-\frac{\left|x - x_i\right|^2}{2\gamma^2}\right) \tag{15}$$

2.5 Optimization algorithms

The evolutionary algorithms that were used to train the ANFIS, ANN, and SVM models are outlined.

2.5.1 Nomadic people algorithm (NPA)

Nomads are people who move from one place to another. The new algorithm was inspired by the lifestyle of the Bedouins (Salih and Alsewari 2019). There are two types of Bedouin families, namely, sheikhs and normal families. A sheikh is the leader of a tribe. Normal families can take the lead if they become more influential than the sheikh's family (Salih and Alsewari 2019). The living location for the families is determined by the sheikh (Salih and Alsewari 2019). Families are sent by the sheikh to find the best living location. When a family finds a good location, the sheikh moves towards the best position. The normal families then establish their tents in a semi-circular shape around the sheikh's tent (Salih and Alsewari 2019).

The NPA has five main levels: initial meeting, semi-circular distribution, families searching, leadership transition, and periodical meetings. First, a set of leaders is initialized by the following equation (Fig. 4).

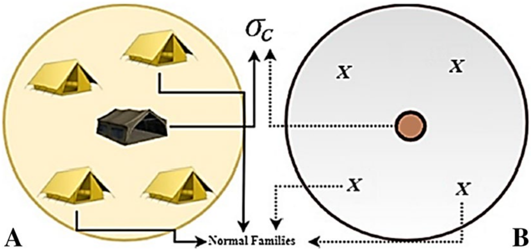

Fig. 4 The Semicircular distribution of the families (Salih and Alsewari 2019)

(1) Initial meeting (Salih and Alsewari 2019):

A leader shows the local optimum solution in the NPA:

$$\vec{\sigma}_c = \left(U_B - L_B\right) \times \text{rand} + L_B \tag{16}$$

where U_B is the upper bound;L_B is the lower bound; rand is a random number; and $\vec{\sigma}_c$ is the location of clan c as a leader.

(2) Semi-circular distribution:

(x) is initiated as a family set that is randomly distributed within a circle with a predefined radius. A semi-circular distribution is modelled as follows (Salih and Alsewari 2019):

$$\begin{aligned} X &= \left(R_d \times \sqrt{R_1}\right) \times \cos(\theta) + X_0 \\ Y &= \left(R_d \times \sqrt{R_2}\right) \times \cos(\theta) + Y_0, \end{aligned} \tag{17}$$

where X and Y are the coordinates of new solutions; X_0 and Y_0 are the coordinates of the centre of the circle; R_1 and R_2 are random parameters; R is the known radius; and θ is the angle value of a solution (in [0, 2π]). However, there was a concern related to any X and Y coordinates within the search space. Thus, Eq. (17) was rewritten as follows (Salih and Alsewari 2019):

$$\vec{X}_c = \vec{\sigma}_c \times \sqrt{R} \times \cos\theta \tag{18}$$

where $\vec{X}_c$ is the family position; $\vec{\sigma}_c$ is the clan leader and swarm location; and R is a random number in the range [0,1]. Figure 4 shows the semi-circular distribution of the families.

(1) Families searching:

The families use the families searching (exploration part) operator to find better locations far from the local best solution (Salih and Alsewari 2019):

$$\vec{X}_i^{\text{new}} = \vec{X}_i^{\text{old}} + \left(a_c * \left(\overrightarrow{\left(\sigma_c - X_i^{\text{old}}\right)}\right) \oplus Levy\right) \tag{19}$$

where $\vec{X}_i^{\text{new}}$ is the new position; $\vec{X}_i^{\text{old}}$ is the old position; and a_c is the representation of distances (average) for the set of normal families and σ_c.

$$a_c = \frac{\sum_{i=1}^{\varphi} \sqrt{\left(\vec{\sigma}_c - X_i^{\text{old}}\right)}}{\psi} \tag{20}$$

The *Levy* flight provides the random walk as follows:

$$Levy \sim u = t^{-\lambda} \tag{21}$$

Leadership transition:
The family with the best objective function becomes the new leader.

(1) Periodical meetings:

The leaders help in solving any problems during this period. The most powerful leader is determined in the periodical meetings. The most powerful leader suggests updating to the locations as alternative solutions for the rest of the sheikhs; such a step could be carried out as follows:

$$\Delta\text{pso} = \psi\left(\frac{\sqrt{\sum_i^D \left(\sigma^E - \sigma_C^N\right)^2}}{\neq D}\right), \tag{22}$$

where σ^E is the position of the best leader; σ_C^N is the normal leader's position; D is the problem dimensions; ψ is the direction; and Δpso is the normalized distance between the normal leaders and the top ones; ψ (the direction of the variables) is used to guide the normal leaders:

$$\psi = \begin{bmatrix} 1 & (if)\left(\sigma^E\right) \geq 0 \\ -1 & \leftarrow \text{Otherwise} \end{bmatrix} \tag{23}$$

The updated position of the normal leader is as follows:

$$\vec{\sigma}_c^{\text{new}} = \vec{\sigma}_c^N + \Delta\text{pos}\left(\sigma^E - \sigma_c^N\right) * \frac{IT}{\neq T}, \tag{24}$$

where σ_c^N is the old location of the normal leader; and $\vec{\sigma}_c^{\text{new}}$ is the new location of the normal leader. The swarms use the periodical meetings to share their information, which is called a meeting room approach. The meeting room approach is used to increase the convergence speed. Figure 5 shows the flowchart of the NPA. The random parameters of the NPA can be found using the Taguchi model.

2.5.2 Bat Algorithm (BA)

The BA is widely utilized for big data sensing (Cui et al. 2019), load–frequency controller designs (Abd-Elazim and Ali 2016), vehicle routing (Zhou et al. 2016), multi-objective

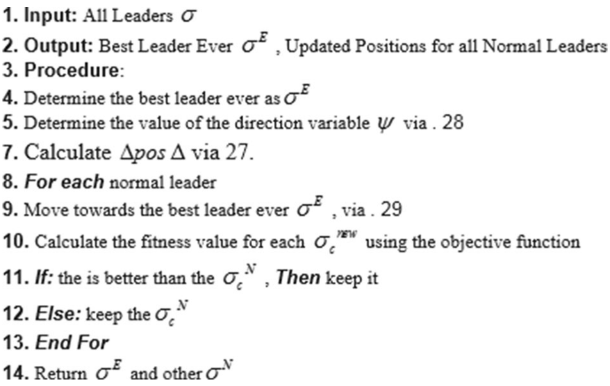

```
1. Input: All Leaders $\sigma$
2. Output: Best Leader Ever $\sigma^E$ , Updated Positions for all Normal Leaders
3. Procedure:
4. Determine the best leader ever as $\sigma^E$
5. Determine the value of the direction variable $\psi$ via . 28
7. Calculate $\Delta pos\,\Delta$ via 27.
8. For each normal leader
9. Move towards the best leader ever $\sigma^E$ , via . 29
10. Calculate the fitness value for each $\sigma_c^{new}$ using the objective function
11. If: the is better than the $\sigma_c^N$ , Then keep it
12. Else: keep the $\sigma_c^N$
13. End For
14. Return $\sigma^E$ and other $\sigma^N$
```

Fig. 5 The flowchart of NPA

optimization (Tharakeshwar et al. 2017), and image compression (Karri and Jena 2016). One of the main advantages of the BA is that it can provide a quick convergence.

The BA was inspired by the echolocation system of bats. Each bat shows one possible solution. Bats use the echolocation system to identify the difference between a prey and obstacles. Bats adjust their signal bandwidth. The velocity, position, and frequency of each bat are updated as follows (Cui et al. 2019):

$$f_i = f_{\min} + \left(f_{\max} - f_{\min}\right)\beta \tag{25}$$

$$v_i^t = v_i^{t-1} + \left(x_i^{t-1} - x^*\right)f_i \tag{26}$$

$$x_i^t = x_i^{t-1} + v_i^t \tag{27}$$

where f_i is the frequency of the ith bat; $f_{\max}$ is the maximal frequency; $f_{\min}$ is the minimal frequency; x_i^{t-1} is the position of the ith bat at iteration $t-1$; v_i^{t-1} is the velocity of the ith bat at iteration $t-1$; and x^* is the current global best solution found so far. The random walk is used to provide a new solution for each bat:

$$x_{\text{new}} = x_{\text{old}} + \varepsilon A_t, \tag{28}$$

where ε is a random number; x_{new} is the new position; x_{old} is the old position; and A_t is the average loudness of the bats. When a prey is spotted by the bats, the bats decrease their loudness and increase the pulsation rate:

$$A_i^{t+1} = \mu A_i^t, r_i^{t+1} = r_i^0\left[1 - \exp\left(-\gamma t\right)\right], \tag{29}$$

where r_i^0 is the initial pulse;μ is the pulse frequency; A_i^{t+1} is the loudness of the ith bat at iteration t; and γ is the pulse amplitude attenuation coefficient. Figure 6 shows the BA flowchart. The key parameters of the BA can be obtained from the Taguchi model.

2.5.3 Krill Algorithm (KA)

The KA was inspired by the behaviour of krill swarms in the sea. The KA is widely used for structural seismic reliability evaluations (Asteris et al. 2019), feature selections (Abualigah 2019), and economic dispatch solutions (Pulluri et al. 2019). One of the advantages of the krill algorithm is the avoidance of local optima. The algorithm updates the position of each krill on the basis of three behaviours, as follows:

$$\frac{\mathrm{d}x_i}{\mathrm{d}t} = N_i + F_i + D_i \tag{30}$$

where x_i is the krill position; N_i is the other's movement effect; F_i is the foraging behaviour; and D_i is the random physical diffusion.

To determine the direction of a motion-induced krill ρ_i by other krill individuals

$$N_i^{\text{new}} = N_i^{\max}\rho_i + \omega_n N_i^{\text{old}} \tag{31}$$

where $N_i^{\max}$: the extreme induced speed, ω_n: the inertia weight of the motion-induced krill, and N_i^{old}: the last motion-induced krill.

The previous experiences about food locations are then used to model the foraging motion:

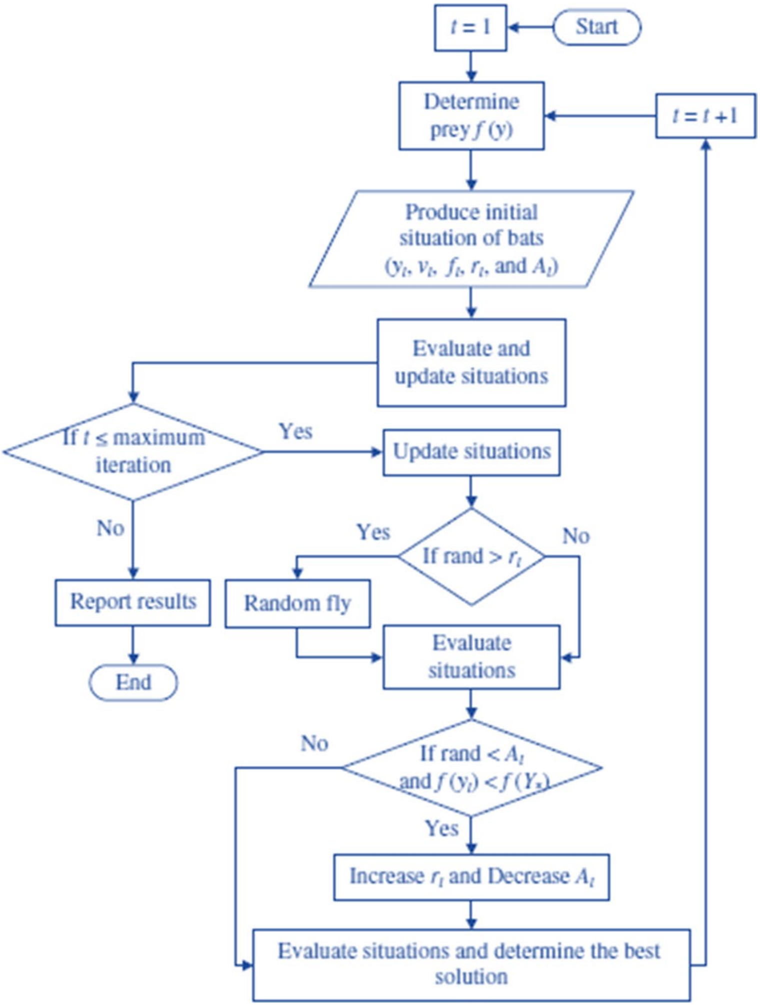

Fig. 6 Flowchart of bat algorithm (Bozorg-Haddad et al. 2015)

$$\begin{aligned} F_i &= V_f \beta_i + \omega_f F_i^{\mathrm{old}} \\ \beta_i &= \beta_i^{\mathrm{food}} + \beta_i^{\mathrm{best}} \end{aligned} \tag{32}$$

where V_f is the speed of foraging; ω_f is the inertia weight of the foraging motion; β_i^{food} is the food attraction;F_i^{old} is the last foraging motion; and β_i^{best} is the best food attraction.

Physical diffusion is considered as a random search process

$$D_i = D^{\max} \delta \tag{33}$$

where $D^{\max}$ is the extreme diffusion speed; and δ is a random number.

The position of the krill can be updated on the basis of the three above-mentioned behaviours:

$$X_i(t + \Delta t) = X_i(t) + \Delta t \frac{\mathrm{d}X_i}{\mathrm{d}t}, \tag{34}$$

where $X_i(t + \Delta t)$ is the new krill position; $X_i(t)$ is the krill position; and Δt is the time interval. Figure 7 shows the KA flowchart.

2.5.4 Salp Swarm Algorithm (SSA)

The SSA is a nature-inspired optimization procedure algorithm that represents the swarming behaviour of salps (Mirjalili et al. 2017). Salps often create a swarm called a salp chain. The salp chain helps salps during the foraging process. The swarm is guided by the leader salp, and followers pursue the leader and other salps (Mirjalili et al. 2017). The leader moves in the direction of a food source. Population initialization is the first level in the SSA. The initial position of salps is randomly initialized. Then, the objective function of each salp is calculated, and the variable F as a food source is used to determine the best position among all the salps. Next, the salps will change their position; first, the leader, and then, followed by the rest. For the leader, the position is changed as follows (Mokhtarzad et al. 2017):

$$x_j^1 = \begin{bmatrix} F_j + c_1\left(\left(ub_j - lb_j\right)c_2 + lb_j\right) \leftarrow c_3 \geq 0.5 \\ F_j - c_1\left(\left(ub_j - lb_j\right)c_2 + lb_j\right) \leftarrow c_3 < 0.5 \end{bmatrix}, \tag{35}$$

where x_j^1 is the leader's position; F_j is the food source position in the jth dimension; ub_j and lb_j are the upper and lower bounds of the jth decision variable, respectively; and c_1, $c_{2,}$ and c_3 are random numbers. c_1 is responsible for balancing between exploitation and exploration:

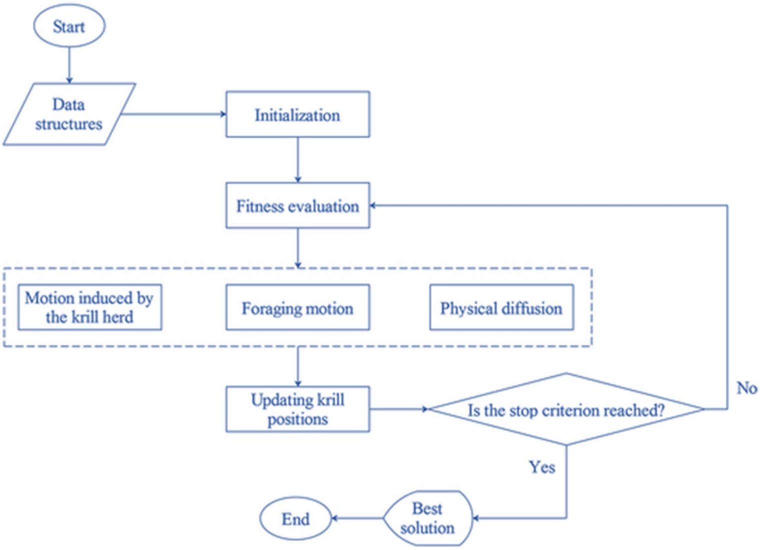

Fig. 7 The flowchart of the krill algorithm

$$c_1 = 2e^{-\left(\frac{4t}{T}\right)^2} \tag{36}$$

where T is the number of epochs; and t is the current iteration. To update the position of each follower, the following equation is used:

$$x_i^j = \frac{1}{2}\left(x_i^j + x_i^{j-1}\right) \tag{37}$$

where x_i^j is the location of the follower salp in the jth dimension. Figure 8 shows the flowchart of the SSA.

2.5.5 Hybrid ANFIS, SVM, MLP, and RBFNN models

The model parameters can be obtained using optimization algorithms. The operator and different levels of optimization algorithms are utilized to obtain the values of the model parameters.

- ANFIS and evolutionary algorithms

The ANFIS model has two kinds of parameters, namely, consequent and premise parameters. The consequent and premise parameters affect the accuracy of the ANFIS model. The assumption of the optimization algorithm is the position of agents that can be considered as the global solution and the model parameters (Muslim et al. 2020; Najah et al. 2012; Najah Ahmed et al. 2019). To train the ANFIS model, evolutionary algorithms are utilized to find the optimal parameter values. Training data are used to start the ANFIS training. A fitness

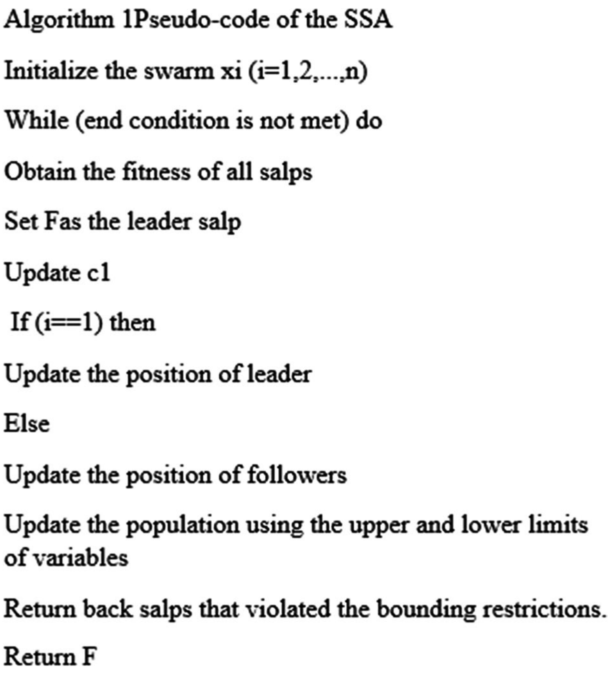

```
Algorithm 1Pseudo-code of the SSA
Initialize the swarm xi (i=1,2,...,n)
While (end condition is not met) do
Obtain the fitness of all salps
Set Fas the leader salp
Update c1
 If (i==1) then
Update the position of leader
Else
Update the position of followers
Update the population using the upper and lower limits
of variables
Return back salps that violated the bounding restrictions.
Return F
```

Fig. 8 Flowchart of SSA

function is defined to measure the prediction error. In this study, the root mean square error (RMSE) was used to calculate the prediction error. The root mean square error is widely used as a fitness function to evaluate different models and algorithms. Agents in the optimization algorithms hold the parameters of the ANFIS model that decision makers want to optimize. Thus, each agent shows the parameters of the ANFIS model. The parameters of the ANFIS model are updated using the operators of optimization algorithms. Finally, the value of the objective function is computed at each iteration.

- MLP and evolutionary algorithms

The accuracy of the MLP model is affected by the weight connection and the bias parameter. In this study, the agents in the optimization algorithms kept the parameters of the MLP model. First, the MLP training starts with the training data. Then, the value of the objective function (RMSE) is computed at each iteration. The initial agent position shows the initial values of the weight and bias parameters. The convergence cycle of the optimization algorithms continues until they achieve the lowest error in the results. Each optimization algorithm has different operators. The operators of the optimization algorithms update the position of the agents (the value of the weight connection and bias parameter).

2.5.5.1 RBFNN and optimization algorithms The centre and width of hidden neurons affect the accuracy of RBFNN models. Each agent in the optimization algorithms holds the parameters of the RBFNN model. The RBFNN training begins by using the training data. The RMSE is computed at each iteration. The parameters of the RBFNN model are updated when each algorithm is updated at each iteration. When the hybrid RBFNN optimization algorithms achieve the lowest error in the results, the simulation and optimization process are completed.

- SVM and optimization algorithms

The γ, C, and ψ parameters affect the accuracy of the SVM model. Agents in the evolutionary algorithms keep the values of the SVM parameters. First, the SVM training starts with the training data. Then, the objective function value is computed at each iteration. The operators of the evolutionary algorithms are utilized to update the value of the SVM parameters. When the position of the agents in the optimization algorithms is updated at each iteration level, the objective function is computed. When the SVM optimization algorithms achieve the lowest error in the results, the simulation optimization process is finished.

3 Case study and data resources

This study predicted droughts over Iran and several sub-regions across Iran in 1980–2014. Figure 9 shows the location of the case study. The different sub-regions were used to show the accuracy of different models for different regions with different climates. The data of 1980 to 2014 were used because they were available for the current study. The chosen regions have separate climatic conditions. The northern region is a subtropical region, whereas the south-eastern part is arid. The north-western region is mountainous with hot summers and cold winters. The south-western part is sub-humid with warm summers,

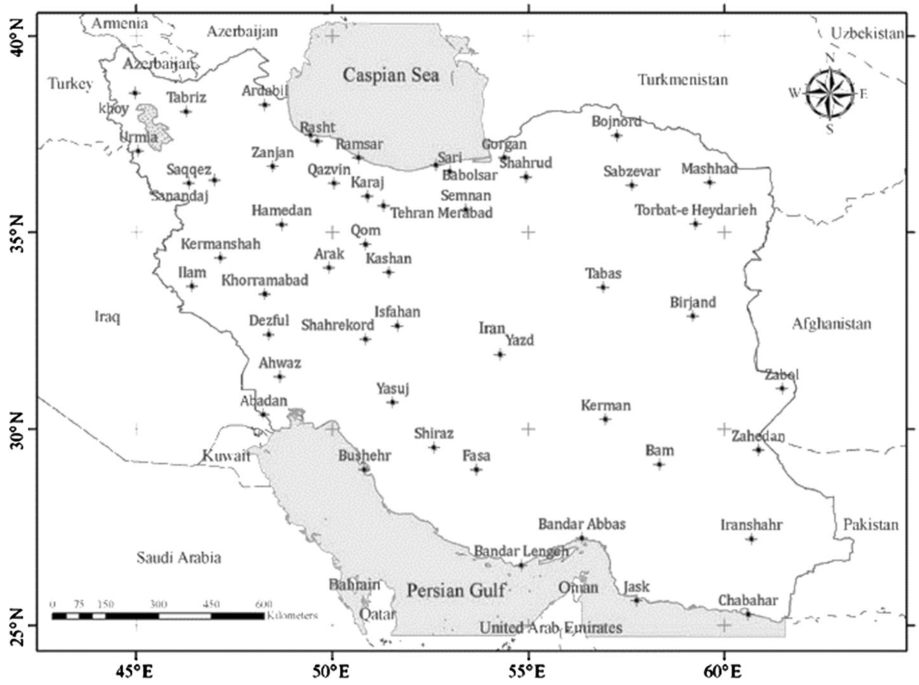

Fig. 9 The Location of Case Study

while the central and north-eastern regions have arid and semiarid climates. McKee et al. (1993) introduced the SPI to forecast droughts. The gamma probability density should be fitted to the total precipitation to evaluate the SPI. If the value of the precipitation is represented by x, the cumulative probability (CP) can be evaluated as follows:

$$G(x) = \int\limits_{0}^{x} g(x)\mathrm{d}x = \frac{1}{\beta^{\alpha}\Gamma(\alpha)} \int_{0}^{x} x^{\alpha-1} e^{-\frac{x}{\beta}} \mathrm{d}x \tag{38}$$

where α is the shape factor; and β is the scale factor. The definition of the cumulative probability changes if x is equal to zero:

$$H(x) = q + (1 - q)G(x) \tag{39}$$

Then, the standard of the normal variable (z) can be achieved through the cumulative probability (CP), which is the SPI value. The SPI can be computed from 1 up to 72 months. The SPI is based on a single variable as the input (precipitation values), so it has a less calculative complexity than that of other drought indices. The purpose of this article was to reflect short- and medium-moisture conditions. The reviewed literature widely used the three-month SPI for the prediction of short- and medium-moisture conditions (Chen et al. 2019). Thus, the current article used the three-month SPI for Iran to have a comprehensive evaluation of short- and medium-term moisture conditions. There are different SPI values for different time intervals but the current study used the 3-month SPI to consider the effects of droughts for short periods. Some random stations were considered to evaluate the ability of hybrid models to model droughts. Different studies indicated that the three-month SPI has the highest correlation with the vegetation response, and is thus the most suitable index for detecting agricultural drought (Satgé et al. 2019; Bayissa et al. 2019). Azarbayjan (northwest Iran), Khouzestan (southwest Iran), Khorasan (northeast Iran), Isfahan (central Iran), and Sistan and Baloucehstan (southeast Iran) were selected for the testing models. These stations were selected because they have different climates. Thus, different models can be evaluated under different climates.

Using the same process for other stations, the spatial distribution and temporal variation maps of the SPI were generated for Iran. In this study, the previous monthly SPI data were used for a one-month-ahead forecast of the SPI:

$$\mathrm{SPI}_t = f(\mathrm{SPI}(t-1), \ldots, \mathrm{SPI}(t-9)) \tag{40}$$

where SPI $(t - 1)$ is the one-month-lagged SPI; and $SPI(t-9)$ is the nine-month-lagged SPI. Figure 10 shows the SPI time series; 80% and 20% of the data were used for the training and testing levels, respectively. The monthly data were collected from 1980 to 2014.

3.1 Input Selection

The selection of appropriate inputs to predict hydrological variables is a real challenge. Literature reviews widely use the principal component analysis (PCA) to find the appropriate input combinations for modelling hydrological variables (Fernandez et al. 2019; Cui et al. 2019). Although different models can be used to find the appropriate inputs, previous studies have confirmed the ability of the PCA in finding the appropriate inputs (Fernandez et al. 2019; Cui et al. 2019). The PCA is a model for decreasing the dimensionality of an input variable by indicating it with a few uncorrelated variables (orthogonal) that capture most of its variability (Lu et al. 2019). Thus, the data size can be decreased by removing the weaker components.

$$Z_i = a_{i1}x_1 + a_{i2}x_2 + \cdots + a_{ip}x_p \tag{41}$$

where Z is the principal component; a_i is the related eigenvectors; and x is the input variable. The eigenvalues are computed as follows:

$$|R - \lambda I| = 0 \tag{42}$$

where I is the unit matrix; and R is the variance–covariance matrix.

3.2 Selection of random parameters

Random parameters have a great impact on the accuracy of evolutionary algorithms. If the random parameters are inappropriately assigned, the algorithms may not converge, and may even be unusable. As the Taguchi model is not highly complex and has many different parameters, it is appropriate for the designing of random parameters (Nobre et al. 2019). Researchers have used the Taguchi model to enhance the accuracy of different models. The Taguchi model uses the signal-to-noise (S/N) ratio to optimize the robustness of the manufacturing process. The S/N ratio is used to measure quality stability, and is computed as follows:

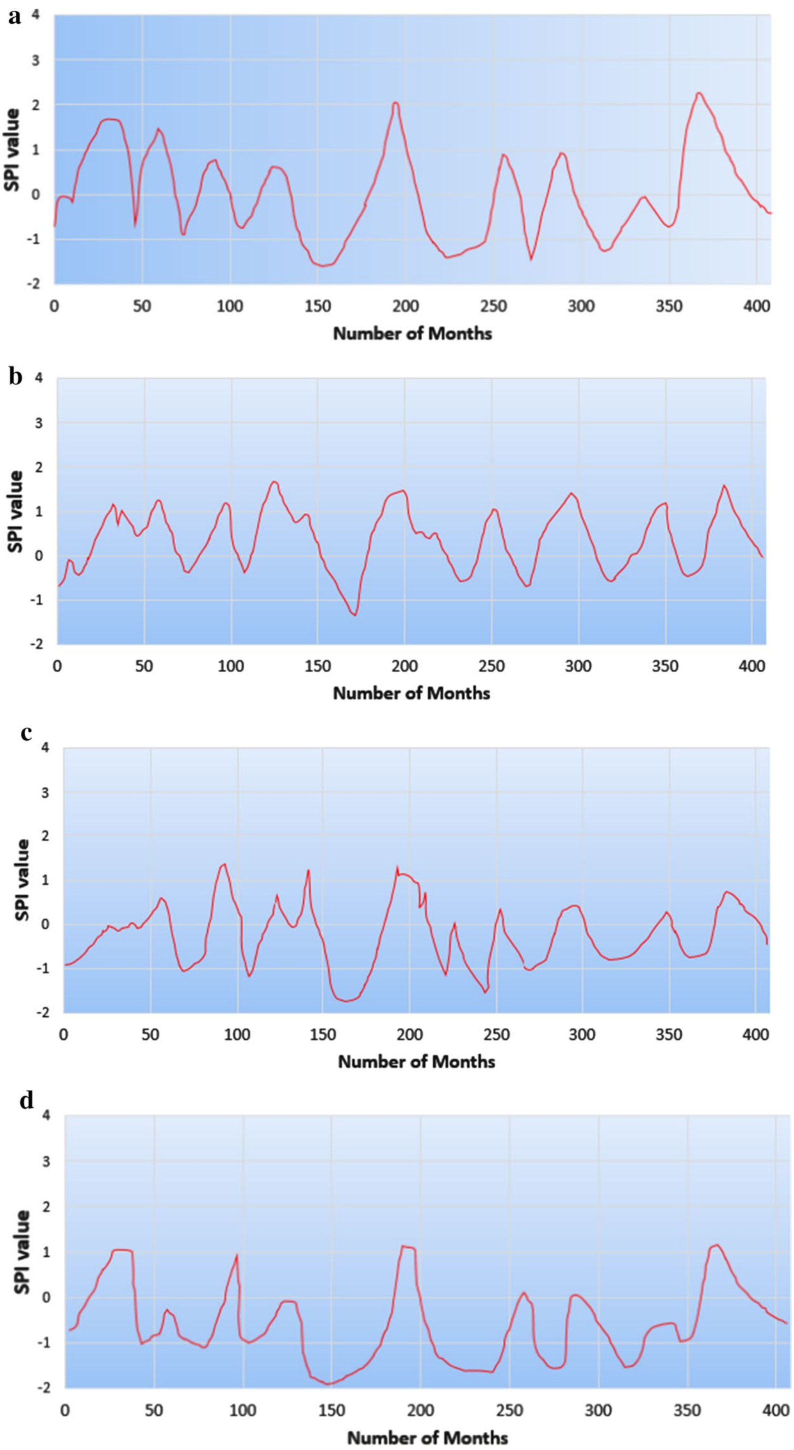

Fig. 10 **a** Time series for Azarbayejan, **b** Khorasan, **c** Sistan and Baloucehstan and **d** Isfahan, **e** Khouzestan, **f** explanation of large climate signals

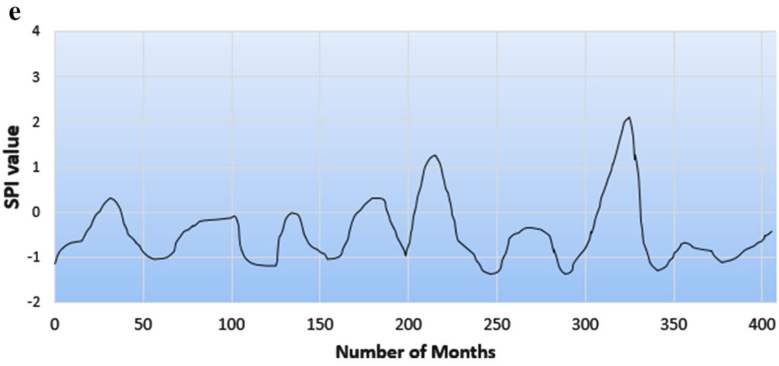

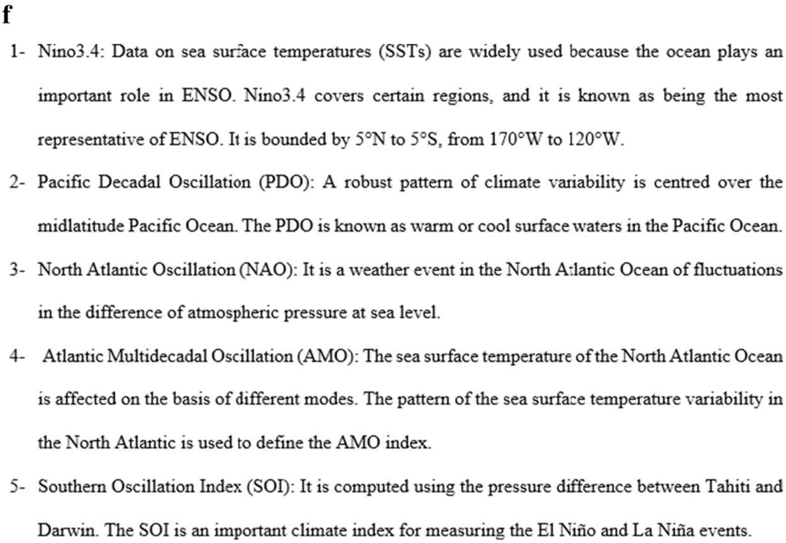

1- Nino3.4: Data on sea surface temperatures (SSTs) are widely used because the ocean plays an important role in ENSO. Nino3.4 covers certain regions, and it is known as being the most representative of ENSO. It is bounded by 5°N to 5°S, from 170°W to 120°W.

2- Pacific Decadal Oscillation (PDO): A robust pattern of climate variability is centred over the midlatitude Pacific Ocean. The PDO is known as warm or cool surface waters in the Pacific Ocean.

3- North Atlantic Oscillation (NAO): It is a weather event in the North Atlantic Ocean of fluctuations in the difference of atmospheric pressure at sea level.

4- Atlantic Multidecadal Oscillation (AMO): The sea surface temperature of the North Atlantic Ocean is affected on the basis of different modes. The pattern of the sea surface temperature variability in the North Atlantic is used to define the AMO index.

5- Southern Oscillation Index (SOI): It is computed using the pressure difference between Tahiti and Darwin. The SOI is an important climate index for measuring the El Niño and La Niña events.

Fig. 10 (continued)

$$\frac{S}{N}\text{ratio} = -10\log_{10}(\text{objective(function)})^2. \tag{43}$$

First, the random parameters of the optimization algorithms are computed. Then, the range of parameters is divided into levels. Since the most important level in the design of an optimization algorithm is the selection of the random parameters, Table 1 lists the random parameters with the defined levels.

In this study, the RMSE was used as an objective function. There are two parameters in the NPA, namely, swarm size and number of maximal iterations. The Taguchi model uses orthogonal arrays to decrease the number of experiments. When four levels for each of the two parameters of the NPA are regarded, 16 experiments should be executed for finding the optimal levels of parameters. By using the Taguchi model for the optimal design, the minimal number of experiments is computed as follows:

$$N = 1 + NV(L - 1) \tag{44}$$

Table 1 The defined levels for different optimization algorithms

NPA

Level	Population size		Maximum number of iterations	
1	100	S/N:2.01	50	S/N:2.16
2	200	S/N:2.21	100	**S/N:2.24**
3	300	**S/N:2.34**	150	S/N:2.12
4	400	S/N:2.14	200	S/N:2.00

BA

Level	Population size		Maximum frequency		Minimum frequency		Maximum loudness		Minimum loudness		Maximum number of iterations	
1	100	S/N:3.12	3	S/N:3.25	1	S/N:3.20	0.30	S/N:3.20	0.10	S/N:3.22	100	S/N:3.12
2	200	S/N:3.15	5	**S/N:3.14**	2	**S/N:3.12**	0.50	**S/N:3.17**	0.20	**S/N:3.14**	200	**S/N:3.10**
3	300	**S/N:3.10**	7	S/N:3.15	3	S/N:3.15	0.70	S/N:3.19	0.30	S/N:3.18	300	S/N:3.15
4	400	S/N:3.14	9	S/N:3.18	4	S/N:3.18	0.90	S/N:3.21	0.40	S/N:3.19	400	S/N:3.18

KA

Level	Population size		$D^{\max}$		V_f		$N_{\max}$		Maximum number of iterations	
1	100	S/N:3.10	0.03	S/N:3.12	0.02	S/N:3.15	0.01	S/N:3.14	100	S/N:3.11
2	200	**S/N:3.07**	0.05	S/N:3.10	0.03	S/N:3.18	0.03	S/N:3.10	200	**S/N:3.09**
3	300	S/N:3.15	0.07	**S/N:3.06**	0.04	**S/N:3:02**	0.05	**S/N:3.09**	300	S/N:3.16
4	400	S/N:3.18	0.09	S/N:3.14	0.05	S/N:3.10	0.07	S/N:3.12	400	S/N:3.14

SSA

Level	Population size		Maximum number of iterations	
1	100	**S/N:3.20**	100	**S/N:3.20**
2	200	S/N:3.01	200	S/N:3.01
3	300	S/N:3.19	300	S/N:3.15
4	400	S/N:3.23	400	S/N:3.18

Bold value shows the optimal value of parameters

where *NV* is the number of parameters; *N* is the number of required experiments; and *L* is the number of levels. Hence, at least seven experiments had to be conducted. Next, experiments were chosen according to the level of combinations. Then, the signal-to-noise (S/N) ratio was used to assess the experimental results. The S/N ratio for each parameter level is shown in Table 1. On the basis of the S/N ratio, the optimal levels of random parameter combinations were detected. The optimal values of the random parameters were shown by the maximal value of the S/N ratio. Although there are different statistical indices for evaluating models, the following indices are widely used because they can evaluate models based on different aspects.

(1)Root mean square error: (RMSE):

$$\mathrm{RMSE} = \sqrt{\frac{1}{N}\sum_{i=1}^{N}\left(\left(\mathrm{SPI}_{\mathrm{bo}}\right) - \left(\mathrm{SPI}_{\mathrm{so}}\right)\right)^{2}}. \tag{45}$$

(2)Mean absolute error (MAE):

$$\mathrm{MAE} = \frac{1}{N}\sum_{i=1}^{N}\left|\mathrm{SP}_{\mathrm{bo}} - \mathrm{SP}_{\mathrm{so}}\right| \tag{46}$$

Nash–Sutcliffe efficiency (NSE):

$$\mathrm{NSE} = 1 - \frac{\sum_{t=1}^{N}\left(\mathrm{SPI}_{\mathrm{bo}} - \mathrm{SPI}_{\mathrm{so}}\right)^{2}}{\sum_{t=1}^{N}\left(S_{\mathrm{so}} - \overline{S}_{\mathrm{so}}\right)^{2}} \tag{47}$$

(3)Percent bias (PBIAS):

$$\mathrm{PBIAS} = \left[\frac{\sum_{i=1}^{n}\left(\mathrm{SPI}_{\mathrm{bo}} - \mathrm{SPI}_{\mathrm{so}}\right) \times 100}{\sum_{i=1}^{n}\left(\mathrm{SPI}_{\mathrm{bo}}\right)}\right] \tag{48}$$

Here, n is the number of data; $\mathrm{SPI}_{\mathrm{bo}}$ is the observed SPI; $\mathrm{SPI}_{\mathrm{so}}$ is the estimated SPI; and $\overline{\mathrm{SPI}}_{\mathrm{so}}$ is the average estimated SPI.

3.3 Understanding the relationship between large-scale climate signals and droughts

A drought is a complex event that is affected by different macroscale atmospheric parameters. Large-scale climate indices have significant effects on drought indices (Araghi et al. 2019; Vazifehkhah and Kahya 2019). Previous studies indicated the notable effects of large-scale climate indices on agricultural and meteorological droughts (Wang et al. 2019; Vazifehkhah and Kahya 2019; Nobre et al. 2019). Various researchers have tried to find the relationship between large-scale climate signals and drought indices (Gibson et al. 2019). In this study, the following indices were used to show the effects of large-scale climate indices on droughts (Wang et al. 2019; Vazifehkhah and Kahya 2019; Nobre et al. 2019).

In recent years, researchers have widely used wavelet coherence to identify the relationship between large-scale climate indices and hydrological variables. Tamaddun et al. (2017) used wavelet coherence to find the relationship between large-scale climate signals and streamflow. The results indicated that the ENSO changed streamflow patterns. Joshi et al. (2016) used the continuous wavelet transform to analyse significant periods of variability associated with drought indices. Manzano et al. (2019) used wavelet power spectra to analyse the relationship between climate patterns and drought indices. Wavelet coherence is defined as follows:

$$R_t^2 = \frac{\left|S\left(W_t^{xy}\right)(s)^2\right|}{S\left(s^{-1}\left|W_t^x\right|^2\right) \cdot S\left(s^{-1}\left|W_t^y(s)\right|^2\right)} \tag{49}$$

where W_t^x and W_t^y are the wavelet transforms of time series x and y, respectively; S is the smoothing operator in the time–frequency (scale) domain; $\left(W_t^{xy}\right)$ is the amount of joint power between $x(t)$ and $y(t)$; s is the frequency; and R_t^2 is the wavelet coherence of the two time series, x and y.

$$W^{x,y}(s,\tau) = \frac{1}{\tau}.W^x(s,\tau).W^y(s,\tau) \tag{50}$$

where τ is the time.

4 Discussion and results

4.1 PCA method outputs

Table 2a shows the factor loading and variance contribution for PCA. The modelling results in the Azarbayejan station indicated that the first three principal component variances summed up a contribution rate of 93%; the first principal component (PC) had a contribution of 57%. In the first four principal components, SPI ($t-1$), ($t-2$), and ($t-3$) had relatively large contributions. According to the calculated percentage of the total cumulative variance of more than 91%, the first four PCs were selected for the Khorasan station (Table 2b). The first four principal components provided good correlations with SPI ($t-1$), ($t-2$), and ($t-3$). In Sistan and Balouchestan, the four principal component variances summed up a contribution rate of 97%; the first PC had a contribution of 54% (Table 2c). In the first four principal components, SPI ($t-1$), ($t-2$), ($t-3$), and ($t-4$) had relatively large contributions. In Isfahan, the results indicated that the first four principal components described 97% of variance and provided good correlations with SPI ($t-1$), ($t-2$), ($t-3$), and ($t-4$) (Table 2d). In Khouzestan, the results indicated that the first three principal components described 90% of variance and provided good correlations with SPI ($t-1$), ($t-2$), ($t-3$), and ($t-4$) (Table 2e).

4.2 Analysis results of new hybrid soft computing models

Table 3 shows the performance of the models at the training level. The modelling results in the Azarbayjan station indicated that the RMSE values were in the range of 1.12–1.67, 1.34–1.69, 1.38–1.71, and 1.41–1.73 for the hybrid (ANFIS–NPA, ANFIS–SSA, ANFIS–KA, and ANFIS–BA) and standalone ANFIS models, hybrid and standalone MLP models, hybrid and standalone RBFNN models, and hybrid and standalone SVM models, respectively. Table 3 clearly shows that the ANFIS–NPA showed the best performance compared to the other models. According to the calculated results of the Azarbayjan station, the NSE was 0.93, 0.86, 0.85 and 0.83 for the ANFIS–NPA, MLP–NPA, RBFNN–NPA, and SVM–NPA, respectively. The performance indicators of the hybrid ANFIS, SVM, MLP, and RBFNN indicated that the hybrid soft computing models gave a better performance than the standalone MLP, RBFNN, ANFIS, and SVM models. As observed in Table 3, the NPA had a better accuracy than the SSA, KA, and BA.

The modelling results in the Khorasan station indicated that MAE values were in the range of 1.12–1.67, 1.33–1.63, 1.39–1.63, and 1.40–1.74 for the standalone and hybrid models of ANFIS, MLP, RBFNN, and SVM, respectively. The ANFIS–NPA model enhanced the RMSE performance over the MLP–, RBFNN–NPA, and SVM–NPA by 18%, 22%, and 24%, respectively. The NSE accuracy was seen to increase from 0.87 (ANFIS

Table 2 The Results of principal components for different stations

PC	SP ($t-1$)	SP ($t-2$)	SP ($t-3$)	SP ($t-4$)	SP ($t-5$)	SP ($t-6$)	SP ($t-7$)	SP ($t-8$)	SP ($t-9$)
Azarbayejan (2a) (each cell show the Eigenvalues)									
1	**0.93**	**0.91**	**0.90**	0.89	0.88	0.82	0.78	0.76	0.69
2	**0.92**	**0.92**	**0.89**	0.87	0.86	0.80	0.77	0.74	0.68
3	**0.91**	**0.91**	**0.87**	0.85	0.85	0.79	0.76	0.73	0.67
4	**0.90**	**0.90**	**0.86**	0.84	0.84	0.78	0.75	0.70	0.65
5	0.84	0.83	0.85	0.81	0.82	0.77	0.73	0.69	0.62
6	0.82	0.82	0.84	0.80	0.81	0.76	0.71	0.68	0.60
7	0.81	0.81	0.83	0.79	0.80	0.75	0.70	0.67	0.59
8	0.80	0.80	0.80	0.78	0.79	0.74	0.69	0.62	0.57
9	0.79	0.78	0.77	0.76	0.77	0.72	0.68	0.60	0.56
Contribution of principal components	5.12 PC (1)	1.78 PC (2)	1.5 PC (3)	0.30 PC (4)	0.15 PC (5)	0.07 PC (6)	0.05 PC (7)	0.02 PC (8)	0.01 PC (9)
Khorasan (2b)									
1	**0.94**	**0.93**	**0.92**	0.90	0.87	0.86	0.77	0.74	0.67
2	**0.93**	**0.91**	**0.90**	0.88	0.85	0.84	0.76	0.72	0.66
3	**0.92**	**0.89**	**0.89**	0.86	0.83	0.80	0.75	0.71	0.65
4	**0.90**	**0.87**	**0.87**	0.85	0.84	0.78	0.74	0.70	0.64
5	0.83	0.82	0.86	0.81	0.81	0.76	0.72	0.69	0.63
6	0.81	0.81	0.85	0.80	0.80	0.75	0.71	0.68	0.60
7	0.80	0.80	0.84	0.78	0.80	0.74	0.70	0.66	0.58
8	0.80	0.79	0.83	0.77	0.79	0.73	0.68	0.65	0.56
9	0.78	0.77	0.80	0.75	0.78	0.71	0.67	0.64	0.55
Contribution of principal components	4.87 PC (1)	2.32 PC (2)	1.0 PC (3)	0.40 PC (4)	0.30 PC (5)	0.06 PC (6)	0.03 PC (7)	0.02 PC (8)	0.01 PC (9)
Sistan and Baloucehstan (2c)									
1	**0.93**	**0.93**	**0.90**	**0.89**	0.86	0.85	0.77	0.73	0.66
2	**0.92**	**0.91**	**0.89**	**0.87**	0.84	0.83	0.75	0.71	0.65

Table 2 (continued)

PC	SP ($t-1$)	SP ($t-2$)	SP ($t-3$)	SP ($t-4$)	SP ($t-5$)	SP ($t-6$)	SP ($t-7$)	SP ($t-8$)	SP ($t-9$)
3	**0.91**	**0.89**	**0.87**	**0.85**	0.82	0.82	0.74	0.70	0.64
4	**0.90**	**0.87**	**0.86**	**0.84**	0.81	0.81	0.73	0.69	0.63
5	0.84	0.83	0.85	0.81	0.80	0.80	0.71	0.68	0.62
6	0.82	0.82	0.84	0.80	0.79	0.78	0.70	0.67	0.61
7	0.81	0.81	0.83	0.78	0.78	0.77	0.69	0.65	0.57
8	0.79	0.80	0.82	0.77	0.77	0.76	0.68	0.64	0.55
9	0.78	0.79	0.80	0.74	0.76	0.75	0.67	0.63	0.54
Contribution of principal components	4.86 PC (1)	2.00 PC (2)	1.0 PC (3)	0.95 PC (4)	0.08 PC (5)	0.06 PC (6)	0.03 PC (7)	0.01 PC (8)	0.01 PC (9)
Isfahan (2d)									
1	**0.92**	**0.91**	**0.87**	**0.82**	0.80	0.77	0.65	0.62	0.59
2	**0.91**	**0.90**	**0.86**	**0.81**	0.79	0.75	0.64	0.61	0.55
3	**0.90**	**0.89**	**0.84**	**0.80**	0.78	0.73	0.63	0.55	0.54
4	**0.87**	**0.86**	**0.83**	**0.79**	0.76	0.72	0.62	0.54	0.52
5	0.84	0.82	0.81	0.75	0.73	0.71	0.61	0.53	0.51
6	0.82	0.81	0.80	0.74	0.72	0.69	0.55	0.51	0.50
7	0.81	0.80	0.79	0.73	0.71	0.68	0.54	0.45	0.42
8	0.80	0.80	0.78	0.71	0.70	0.67	0.52	0.43	0.39
9	0.79	0.79	0.77	0.69	0.67	0.66	0.50	0.42	0.38
Contribution of principal components	3.78 PC (1)	2.65 PC (2)	1.55 PC (3)	0.67 PC (4)	0.20 PC (5)	0.07 PC (6)	0.04 PC (7)	0.02 PC (8)	0.02 PC (9)
Khouzestan (2e)									
1	**0.92**	**0.91**	**0.90**	**0.87**	0.82	0.80	0.78	0.76	0.75
2	**0.91**	**0.90**	**0.89**	**0.86**	0.80	0.78	0.77	0.75	0.74
3	**0.90**	**0.89**	**0.87**	**0.85**	0.78	0.76	0.75	0.74	0.72
4	0.89	0.87	0.86	0.82	0.77	0.75	0.74	0.73	0.71

Table 2 (continued)

PC	SP ($t-1$)	SP ($t-2$)	SP ($t-3$)	SP ($t-4$)	SP ($t-5$)	SP ($t-6$)	SP ($t-7$)	SP ($t-8$)	SP ($t-9$)
5	0.87	0.86	0.85	0.80	0.76	0.74	0.73	0.72	0.70
6	0.86	0.85	0.84	0.78	0.75	0.73	0.72	0.71	0.69
7	0.84	0.83	0.83	0.76	0.74	0.72	0.70	0.69	0.67
8	0.82	0.82	0.82	0.75	0.73	0.71	0.69	0.68	0.65
9	0.81	0.81	0.81	0.70	0.69	0.70	0.67	0.67	0.62
Contribution of principal components	**4.58** **PC (1)**	**2.12** **PC (2)**	**1.40** **PC (3)**	0.50 **PC (4)**	0.20 **PC (5)**	0.07 **PC (6)**	0.05 **PC (7)**	0.04 **PC (8)**	0.04 **PC (9)**

Table 3 Analysis training results for new hybrid ANN, ANFIS and SVM models. (a) training results

Model	Azarbayejan					Khorasan				
	RMSE	MAE	NSE	PBIAS	R^2	RMSE	MAE	NSE	PBIAS	R^2
(a)										
ANFIS–NPA	1.12	1.09	0.93	0.12	0.95	1.1	1.12	0.92	0.14	0.94
ANFIS–SSA	1.32	1.28	0.91	0.15	0.90	1.34	1.32	0.90	0.16	0.92
ANFIS–KA	1.45	1.41	0.90	0.16	0.89	1.47	1.43	0.89	0.18	0.90
ANFIS–BA	1.55	1.52	0.89	0.18	0.87	1.56	1.54	0.87	0.19	0.89
ANFIS	1.67	1.65	0.87	0.20	0.85	1.68	1.67	0.87	0.22	0.87
MLP–NPA	1.34	1.32	0.92	0.14	0.93	1.35	1.33	0.91	0.15	0.92
MLP-SSA	1.39	1.37	0.90	0.17	0.89	1.40	1.38	0.89	0.18	0.90
MLP-KA	1.49	1.45	0.89	0.19	0.88	1.50	1.44	0.88	0.21	0.89
MLP-BA	1.57	1.55	0.87	0.21	0.86	1.59	1.53	0.87	0.23	0.86
MLP	1.69	1.64	0.86	0.23	0.85	1.70	1.63	0.85	0.24	0.84
RBFNN–NPA	1.38	1.37	0.91	0.25	0.90	1.42	1.39	0.90	0.25	0.93
RBFNN–SSA	1.42	1.40	0.90	0.27	0.87	1.45	1.41	0.89	0.28	0.91
RBFNN–KA	1.51	1.49	0.88	0.28	0.84	1.53	1.50	0.87	0.29	0.90
RBFNN–BA	1.61	1.52	0.87	0.32	0.83	1.63	1.51	0.86	0.33	0.89
RBFNN	1.71	1.65	0.85	0.33	0.82	1.74	1.63	0.85	0.35	0.83
SVM–NPA	1.41	1.38	0.90	0.25	0.89	1.44	1.40	0.89	0.27	0.89
SVM–SSA	1.44	1.40	0.86	0.29	0.88	1.45	1.42	0.84	0.31	0.87
SVM–KA	1.53	1.50	0.85	0.34	0.87	1.59	1.53	0.83	0.35	0.86
SVM–BA	1.65	1.58	0.84	0.36	0.82	1.69	1.63	0.82	0.38	0.82
SVM	1.73	1.65	0.83	0.37	0.81	1.78	1.74	0.81	0.39	0.80

Model	Isfahan					Sistan and Baloucehstan				
	RMSE	MAE	NSE	PBIAS	R^2	RMSE	MAE	NSE	PBIAS	R^2
ANFIS–NPA	1.16	1.10	0.92	0.14	0.93	1.29	1.27	0.91	0.16	0.92
ANFIS–SSA	1.35	1.29	0.90	0.15	0.90	1.32	1.31	0.90	0.17	0.90
ANFIS–KA	1.39	1.42	0.89	0.17	0.89	1.35	1.32	0.89	0.19	0.89
ANFIS–BA	1.52	1.54	0.87	0.18	0.87	1.37	1.35	0.87	0.21	0.86
ANFIS	1.65	1.67	0.86	0.21	0.85	1.39	1.37	0.85	0.24	0.85
MLP–NPA	1.34	1.33	0.91	0.16	0.89	1.32	1.39	0.90	0.19	0.89
MLP-SSA	1.40	1.38	0.89	0.18	0.88	1.31	1.30	0.87	0.21	0.87
MLP-KA	1.47	1.42	0.87	0.20	0.87	1.34	1.32	0.86	0.23	0.86
MLP-BA	1.55	1.52	0.86	0.22	0.86	1.37	1.35	0.85	0.25	0.85
MLP	1.67	1.63	0.85	0.24	0.84	1.33	1.37	0.83	0.27	0.82
RBFNN–NPA	1.39	1.35	0.91	0.22	0.88	1.47	1.42	0.89	0.21	0.84
RBFNN–SSA	1.44	1.41	0.90	0.26	0.87	1.51	1.46	0.80	0.23	0.88
RBFNN–KA	1.53	1.50	0.87	0.27	0.86	1.53	1.51	0.79	0.27	0.87
RBFNN–BA	1.62	1.53	0.86	0.35	0.85	1.55	1.52	0.77	0.29	0.86
RBFNN	1.74	1.62	0.85	0.37	0.82	1.57	1.54	0.76	0.31	0.83
SVM–NPA	1.43	1.37	0.89	0.29	0.86	1.39	1.51	0.87	0.32	0.86
SVM–SSA	1.49	1.42	0.85	0.31	0.84	1.55	1.53	0.81	0.34	0.85
SVM–KA	1.55	1.49	0.84	0.35	0.83	1.59	1.57	0.78	0.36	0.84
SVM–BA	1.67	1.55	0.83	0.37	0.82	1.61	1.58	0.77	0.37	0.83

Table 3 (continued)

Model	Isfahan					Sistan and Baloucehstan				
	RMSE	MAE	NSE	PBIAS	R^2	RMSE	MAE	NSE	PBIAS	R^2
SVM	1.78	1.63	0.82	0.39	0.80	1.63	1.60	0.75	0.39	0.82

Model	Khouzestan				
	RMSE	MAE	NSE	PBIAS	R^2
ANFIS–NPA	2.25	2.21	0.92	0.14	0.94
ANFIS–SSA	2.27	2.23	0.91	0.16	0.93
ANFIS–KA	2.29	2.25	0.90	0.18	0.89
ANFIS–BA	2.31	2.26	0.87	0.20	0.87
ANFIS	2.33	2.27	0.84	0.22	0.85
MLP–	2.35	2.29	0.90	0.24	0.92
MLP-SSA	2.36	2.31	0.89	0.27	0.90
MLP-KA	2.38	2.34	0.88	0.29	0.88
MLP-BA	2.39	2.37	0.87	0.30	0.85
MLP	2.40	2.38	0.86	0.32	0.83
RBFNN–NPA	2.37	2.32	0.85	0.33	0.89
RBFNN–SSA	2.41	2.36	0.83	0.34	0.88
RBFNN–KA	2.43	2.40	0.81	0.35	0.87
RBFNN–BA	2.45	2.41	0.80	0.36	0.84
RBFNN	2.47	2.43	0.79	0.37	0.89
SVM–NPA	2.39	2.37	0.75	0.38	0.88
SVM–SSA	2.41	2.40	0.73	0.40	0.87
SVM–KA	2.45	2.42	0.71	0.42	0.86
SVM–BA	2.47	2.43	0.70	0.43	0.85
SVM	2.49	2.47	0.69	0.44	0.82

model) to 0.92 (ANFIS–NPA), 0.85 (MLP) to 0.91 (MLP–), 0.85 (RBFNN) to 0.90 (RBFNN–NPA), and 0.81 (SVM) to 0.89 (SVM–NPA).

The ANFIS–NPA model clearly had the best accuracy when compared to the other models in the Isfahan station. According to the calculated results of the Isfahan station, the maximal RMSE values were 1.65, 1.67, 1.74, and 1.78 for the ANFIS, MLP, RRFNN, and SVM models, respectively. The results indicated the superiority of the NPA, followed by the SSA, in comparison to the KA and BA.

The results of the Sistan and Balouchestan stations indicated the superiority of the ANFIS–NPA, followed by the MLP–, in comparison to the RBFNN–NPA and SVM–NPA models. The RMSE of the ANFIS–NPA, MLP–NPA, and RBFNN–NPA was 1.29, 1.32, 1.47, and 1.49 at the training level, as reported in Table 4, in the Sistan and Baloucehstan stations.

The results of the Khuzestan station indicated that the RMSE values varied, namely, between 2.25–2.33, 2.35–2.40, 2.37–2.45, and 2.39–2.49 for the standalone and hybrid models of ANFIS, MLP, RBFNN, and SVM, respectively.

The modelling results in the Azarbayejan station indicated that the RMSE values were 2.21–2.30, 2.24–2.35, 2.28–2.39, and 2.32–2.55 for the hybrid and standalone ANFIS models, hybrid and standalone MLP models, hybrid and standalone RBFNN models, and hybrid and standalone SVM models, respectively (Table 4). In the Azarbayejan station, the ANFIS–NPA outperformed the MLP–, RBFNN–NPA, and SVM–NPA models. The highest NSE was achieved using the ANFIS–NPA model. The results indicated that the RMSE values decreased from 2.33 (ANFIS) to 2.23 (ANFIS–NPA); similarly, the MAE and PBIAS decreased from 2.27 (ANFIS) to 2.18 (ANFIS–NPA) and 0.23 (ANFIS) to 0.16 (ANFIS–NPA), respectively in the Khorasan station. On the basis of the statistical indices, the results of the Khorasan station indicated that the NPA model gave the best performance when compared with the other models. The modelling results in the Isfahan station indicated the superiority of the ANFIS–NPA, followed by the MLP–NPA, in comparison to the RBFNN–NPA and SVM–NPA models. The modelling results in the Isfahan station indicated that the SVM model produced the worst NSE value of all the models. The ANFIS–NPA model was the most accurate among all the models in Sistan and Balouchestan. The MAE decreased from 2.30 (ANFIS) to 2.24 (ANFIS–NPA), and the RMSE and PBIAS decreased from 2.34 (ANFIS) to 2.20 (ANFIS–NPA), and 0.25 (ANFIS) to 0.18 (ANFIS–NPA), respectively, in the Sistan and Balouchestan stations. The ANFIS–NPA outperformed the other models in the Khouzestan station Tables 3 and 4 compare the R^2 values of the different models. According to the results, the SVM–NPA model provided a higher R^2 compared to that of the SVM–SSA, SVM–KA, SVM–BA, and SVM models. The results revealed that the standalone and hybrid MLP models provided a higher R^2 value compared to that of the hybrid and standalone RBFNN models in all the stations. The results indicated that the NPA outperformed the SSA, KA, and BA in all the stations. The standalone and hybrid ANFIS models gave the highest R^2 values in all the stations. The RBFNN forecast had a higher R^2 in comparison with that of the hybrid and standalone SVM models.

4.3 Spatial and temporal droughts for Iran

The previous section regarded the performance of soft computing models for drought predictions. In this section, the soft computing models were used to provide the spatial and temporal maps of the three-month SPI in Iran. To evaluate the accuracy level of the provided maps, the receiver operating characteristic (ROC) curve was used. The ROC curve is a graphical model to specify the performance of a classifier (Cohen et al. 2019). The reliability of the proposed models was assessed by classifying the output of the models as true or false. The ROC is a useful index for evaluating the provided maps, while other indices evaluate the models based on their statistical performance. Thus, the ROC can identify the corrected and uncorrected pixels by the predictive models. The ROC method can be used without any mathematical complexities.

$$\begin{aligned} \mathrm{HR} &= \frac{H}{H+M} \\ \mathrm{FAR} &= \frac{F}{F+N}, \end{aligned} \tag{51}$$

where H is the number of true positives (correct predictions of a drought class); M is the number of false negatives (incorrect predictions of the occurrence of drought); F is the number of false positives (incorrect predictions of a drought class when no droughts are observed); and N is the number of true negatives (correct predictions of a drought class when no droughts are observed). The drought classification is shown in Table 5. The latitude, longitude, and lagged SPI values of the stations were used as inputs to the models.

Table 4 Analysis training results for new hybrid ANN, ANFIS and SVM models. (b) testing level

Model	Azarbayejan					Khorasan				
	RMSE	MAE	NSE	PBIAS	R^2	RMSE	MAE	NSE	PBIAS	R^2
(b)										
ANFIS–NPA	2.21	2.15	0.91	0.15	0.92	2.23	2.18	0.90	0.16	0.93
ANFIS–SSA	2.24	2.20	0.90	0.16	0.90	2.25	2.19	0.89	0.19	0.92
ANFIS–KA	2.26	2.22	0.89	0.18	0.87	2.27	2.23	0.88	0.20	0.86
ANFIS–BA	2.30	2.27	0.87	0.19	0.86	2.31	2.25	0.86	0.22	0.85
ANFIS	2.32	2.30	0.85	0.22	0.84	2.33	2.27	0.84	0.23	0.84
MLP–NPA	2.24	2.18	0.89	0.17	0.90	2.25	2.23	0.89	0.17	0.91
MLP-SSA	2.27	2.23	.0.88	0.19	0.87	2.27	2.25	0.86	0.19	0.90
MLP-KA	2.29	2.27	0.86	0.21	0.86	2.29	2.27	0.85	0.23	0.85
MLP-BA	2.35	2.32	0.84	0.23	0.84	2.32	2.29	0.84	0.25	0.84
MLP	2.40	2.35	0.83	0.25	0.82	2.34	2.31	0.82	0.27	0.82
RBFNN–NPA	2.28	2.20	0.88	0.23	0.88	2.28	2.25	0.87	0.28	0.87
RBFNN–SSA	2.35	2.31	0.87	0.27	0.87	2.33	2.28	0.79	0.29	0.85
RBFNN–KA	2.37	2.36	0.86	0.28	0.86	2.36	2.32	0.78	0.31	0.83
RBFNN–BA	2.39	2.38	0.85	0.36	0.85	2.38	2.34	0.76	0.33	0.82
RBFNN	2.44	2.41	0.82	0.38	0.84	2.39	2.36	0.74	0.35	0.80
SVM–NPA	2.32	2.30	0.81	0.30	0.82	2.43	2.27	0.85	0.37	0.79
SVM–SSA	2.45	2.43	0.80	0.33	0.80	2.45	2.31	0.80	0.30	0.78
SVM–KA	2.47	2.45	0.79	0.37	0.79	2.46	2.33	0.76	0.36	0.77
SVM–BA	2.51	2.48	0.78	0.38	0.78	2.48	2.35	0.75	0.39	0.76
SVM	2.55	2.53	0.77	0.40	0.77	2.51	2.37	0.73	0.40	0.75

Model	Isfahan					Sistan and Baloucehstan				
	RMSE	MAE	NSE	PBIAS	R^2	RMSE	MAE	NSE	PBIAS	R^2
ANFIS–NPA	2.23	2.17	0.92	0.16	0.93	2.24	2.20	0.92	0.18	0.91
ANFIS–SSA	2.26	2.22	0.90	0.17	0.90	2.26	2.22	0.89	0.20	0.88
ANFIS–KA	2.27	2.24	0.88	0.19	0.88	2.28	2.26	0.87	0.22	0.87
ANFIS–BA	2.32	2.29	0.86	0.20	0.87	2.32	2.30	0.85	0.23	0.84
ANFIS	2.33	2.32	0.85	0.21	0.86	2.34	2.30	0.83	0.25	0.82
MLP–NPA	2.25	2.19	0.88	0.18	0.89	2.27	2.26	0.88	0.27	0.89
MLP-SSA	2.28	2.25	.0.87	0.20	0.88	2.28	2.27	0.85	0.29	0.86
MLP-KA	2.31	2.28	0.85	0.22	0.86	2.30	2.29	0.84	0.31	0.85
MLP-BA	2.33	2.33	0.83	0.24	0.85	2.33	2.30	0.83	0.33	0.82
MLP	2.43	2.36	0.82	0.26	0.84	2.35	2.33	0.82	0.27	0.81
RBFNN–NPA	2.27	2.21	0.87	0.27	0.88	2.36	2.34	0.80	0.37	0.89
RBFNN–SSA	2.38	2.32	0.86	0.28	0.87	2.37	2.36	0.79	0.39	0.86
RBFNN–KA	2.36	2.37	0.85	0.29	0.84	2.38	2.37	0.77	0.41	0.85
RBFNN–BA	2.41	2.39	0.84	0.37	0.83	2.41	2.38	0.75	0.43	0.84
RBFNN	2.45	2.42	0.81	0.39	0.82	2.42	2.40	0.73	0.44	0.84
SVM–NPA	2.34	2.32	0.80	0.40	0.84	2.45	2.42	0.77	0.39	0.82
SVM–SSA	2.47	2.45	0.79	0.34	0.81	2.47	2.33	0.75	0.41	0.82
SVM–KA	2.48	2.47	0.78	0.38	0.80	2.48	2.36	0.74	0.42	0.81
SVM–BA	2.52	2.49	0.76	0.39	0.79	2.51	2.38	0.73	0.43	0.80

Table 4 (continued)

Model	Isfahan					Sistan and Baloucehstan				
	RMSE	MAE	NSE	PBIAS	R^2	RMSE	MAE	NSE	PBIAS	R^2
SVM	2.56	2.55	0.75	0.42	0.77	2.54	2.41	0.72	0.45	0.79

Model	Khouzestan				
	RMSE	MAE	NSE	PBIAS	R^1
ANFIS–NPA	3.12	2.98	0.90	0.16	0.91
ANFIS–SSA	3.14	2.95	0.89	0.18	0.88
ANFIS–KA	3.17	2.97	0.88	0.20	0.87
ANFIS–BA	3.21	2.98	0.87	0.22	0.86
ANFIS	3.23	3.02	0.86	0.23	0.85
MLP–	3.25	3.11	0.85	0.24	0.89
MLP-SSA	3.27	3.12	0.84	0.28	0.87
MLP-KA	3.29	3.16	0.84	0.34	0.86
MLP-BA	3.32	3.18	0.82	0.38	0.85
MLP	3.35	3.21	0.80	0.39	0.84
RBFNN–NPA	3.37	3.23	0.79	0.40	0.87
RBFNN–SSA	3.39	3.24	0.78	0.45	0.86
RBFNN–KA	3.40	3.24	0.76	0.47	0.85
RBFNN–BA	3.42	3.25	0.75	0.48	0.83
RBFNN	3.44	3.29	0.74	0.52	0.82
SVM–NPA	3.45	3.32	0.72	0.53	0.86
SVM–SSA	3.46	3.35	0.71	0.54	0.85
SVM–KA	3.47	3.36	0.70	0.55	0.80
SVM–BA	3.49	3.39	0.73	0.56	0.79
SVM	3.51	3.42	0.74	0.57	0.77

Figure 11 lists the used stations for providing the drought maps. The PCA model, as in the previous section, was used to select the lagged SPI values for each station. Then, the drought monitor maps were generated using the SPI time series of each station, and the soft computing models. Table 6 shows the computed area under the ROC curve (AUC) for different drought classifications. The number of drought occurrences and non-occurrences were used to compute the HR and FAR. In general, an AUC of 1 shows a perfect model (Fig. 12). The statistical results of the ANFIS–NP model indicated a considerably low error for the different drought classifications in comparison with that of the other models. For extreme droughts, the AUC increased from 0.77 (SVM) to 0.92 (ANFIS–NPA). Regarding severe droughts, the AUC increased from 0.79 (SVM) to 0.94 (ANFI-NPA). The results indicated that the ANFIS–NPA, MLP–, RBFNN–NPA, and SVM–NPA models performed better than the other models. The spatial and temporal drought characteristics are shown in Fig. 13. Maps were provided by the ANFIS–NPA model, which was selected as the best model. Additionally, this study used the innovative trend analysis (ITA), introduced by Sen (2012), to identify drought trends. Unlike other methods, the ITA method does not need any assumptions. The ITA can identify trends without special complexities or special assumptions. Modelers can use the ITA easily for climate events. The first step was

Table 5 The SPI classification

SPI value	Classification
≥ 2	Extremely wet
1.5 to 1.99	Severely wet
1 to 1.49	Moderately wet
0 to 0.99	Mild wet
− 0.99 to 0	Mild drought
− 1.49 to − 1	Moderately drought
1.99 to − 1.5	Severely drought
− 2 >	Extremelv drought

to equally divide the time series into two groups. Then, the groups were placed on the X and Y axes, respectively. No trend could be observed with respect to the time series if the SPI data were placed on the ideal line, while an increasing trend in the time series was observed if the SPI data were placed on the upper triangular area of the ideal line (Sen 2012). A decreasing trend could be observed if the SPI data were collected on the lower triangular area of the ideal line. The AUC plot of the extreme drought classification, as shown in Fig. 15, was presented as a sample of the best model.

With regard to monthly droughts in Iran, an increasing trend was found throughout the studied period in *January*. In February, the results were trendless for $SPI \leq -1$; however, the index followed an increasing trend for $SPI > -1$ (Fig. 14). The application of the ITA method revealed an increasing trend in March. An increasing trend in April was observed for $SPI \leq -1$ and SPI. For May, June, July, and August, although there was a decreasing trend for $SPI \geq 1$, the SPI results indicated an increasing trend for $SPI \leq -1$. The summer months showed an increasing trend for $SPI \leq -1$. The results generally indicated that decision makers should utilize effective strategies for water resource management.

4.4 Wavelet coherence analysis between droughts and large-scale climate signals

Figure 15 shows the wavelet coherence analysis of the three-month SPI in Iran for the period of 1980–2014. For an overall interpretation of the whole country, the duration of each period (i.e., < 4, 4–8, 8–16, 16–32, and 32–64) was summarized on the basis of the duration values gained for any station with a 5% significance level. There was a statistically positive significant correlation between Nino3.4 and the three-month SPI with a 48–65-month signal from 1980 to 2014, and it exhibited a positive correlation with the 26–34-month signal from 2008 to 2014. Figure 15 indicates that the PDO had positive statistical significance with the three-month SPI in Iran with a signal of 32–64 months from 1990 to 1997. Figure 15 demonstrates that the NAO had a statistical significance with the three-month SPI in Iran, with a 60–64-month signal from 1998 to 2014. As observed in Fig. 15, there was a statistical significance between AMO and the three-month SPI, with a 34–59-month signal from 2006 to 2014. The results revealed that there was a statistical significance between SOI and the three-month SPI with a 48–60-month signal from 1998 to 2014. However, the results generally indicated that the climate and geographical data could be used as the input data to the soft computing models. The improved ANFIS model with the reliable data can achieve a high accuracy. A soft computing model with a high ability can predict droughts under different climate change conditions. Thus, the selection of the

Fig. 11 The Location of used stations for providing the spatially and temporally drought map

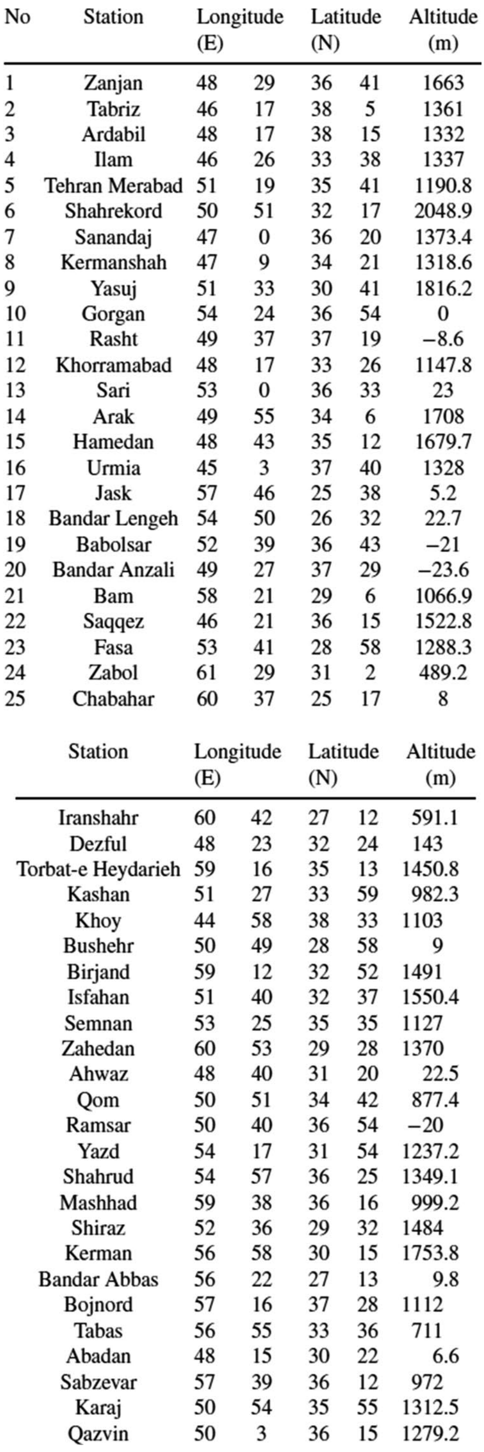

No	Station	Longitude (E)		Latitude (N)		Altitude (m)
1	Zanjan	48	29	36	41	1663
2	Tabriz	46	17	38	5	1361
3	Ardabil	48	17	38	15	1332
4	Ilam	46	26	33	38	1337
5	Tehran Merabad	51	19	35	41	1190.8
6	Shahrekord	50	51	32	17	2048.9
7	Sanandaj	47	0	36	20	1373.4
8	Kermanshah	47	9	34	21	1318.6
9	Yasuj	51	33	30	41	1816.2
10	Gorgan	54	24	36	54	0
11	Rasht	49	37	37	19	−8.6
12	Khorramabad	48	17	33	26	1147.8
13	Sari	53	0	36	33	23
14	Arak	49	55	34	6	1708
15	Hamedan	48	43	35	12	1679.7
16	Urmia	45	3	37	40	1328
17	Jask	57	46	25	38	5.2
18	Bandar Lengeh	54	50	26	32	22.7
19	Babolsar	52	39	36	43	−21
20	Bandar Anzali	49	27	37	29	−23.6
21	Bam	58	21	29	6	1066.9
22	Saqqez	46	21	36	15	1522.8
23	Fasa	53	41	28	58	1288.3
24	Zabol	61	29	31	2	489.2
25	Chabahar	60	37	25	17	8

Station	Longitude (E)		Latitude (N)		Altitude (m)
Iranshahr	60	42	27	12	591.1
Dezful	48	23	32	24	143
Torbat-e Heydarieh	59	16	35	13	1450.8
Kashan	51	27	33	59	982.3
Khoy	44	58	38	33	1103
Bushehr	50	49	28	58	9
Birjand	59	12	32	52	1491
Isfahan	51	40	32	37	1550.4
Semnan	53	25	35	35	1127
Zahedan	60	53	29	28	1370
Ahwaz	48	40	31	20	22.5
Qom	50	51	34	42	877.4
Ramsar	50	40	36	54	−20
Yazd	54	17	31	54	1237.2
Shahrud	54	57	36	25	1349.1
Mashhad	59	38	36	16	999.2
Shiraz	52	36	29	32	1484
Kerman	56	58	30	15	1753.8
Bandar Abbas	56	22	27	13	9.8
Bojnord	57	16	37	28	1112
Tabas	56	55	33	36	711
Abadan	48	15	30	22	6.6
Sabzevar	57	39	36	12	972
Karaj	50	54	35	55	1312.5
Qazvin	50	3	36	15	1279.2

Table 6 The AUC results for different models

Model	Extremely drought	Severely drought	Moderately drought	Mid drought	Mild wet	Moderately wet	Severely wet	Extremely wet
ANFIS–NPA	0.92	0.94	0.93	0.94	0.93	0.94	0.92	0.90
ANFIS–SSA	0.89	0.92	0.91	0.93	0.90	0.93	0.89	0.88
ANFIS–KA	0.88	0.90	0.90	0.92	0.91	0.92	0.86	0.86
ANFIS–BA	0.87	0.89	0.89	0.91	0.89	0.91	0.85	0.84
ANFIS	0.86	0.88	0.86	0.89	0.87	0.90	0.83	0.82
MLP–	0.85	0.87	0.85	0.93	0.90	0.89	0.91	0.89
MLP-SSA	0.84	0.85	0.83	0.92	0.89	0.88	0.89	0.87
MLP-KA	0.83	0.82	0.81	0.91	0.82	0.87	0.86	0.85
MLP-BA	0.78	0.80	0.80	0.90	0.80	0.86	0.83	0.84
MLP	0.77	0.79	0.84	0.89	0.78	0.85	0.80	0.83
RBFNN–NAP	0.85	0.87	0.91	0.90	0.89	0.84	0.89	0.90
RBFNN–SSA	0.84	0.86	0.90	0.89	0.88	0.83	0.88	0.89
RBFNN–KA	0.83	0.84	0.89	0.88	0.87	0.82	0.87	0.87
RBFNN–BA	0.82	0.80	0.87	0.87	0.85	0.81	0.86	0.86
RBFNN	0.80	0.76	0.86	0.86	0.84	0.80	0.85	0.84
SVM–NPA	0.84	0.85	0.85	0.84	0.83	0.78	0.84	0.83
SVM–SSA	0.81	0.83	0.84	0.80	0.82	0.76	0.82	0.80
SVM–KA	0.80	0.81	0.80	0.78	0.80	0.74	0.80	0.78
SVM–BA	0.79	0.80	0.79	0.76	0.78	0.70	0.78	0.76
SVM	0.77	0.79	0.78	0.72	0.76	0.68	0.76	0.74

Fig. 12 The schematic of ROC curve

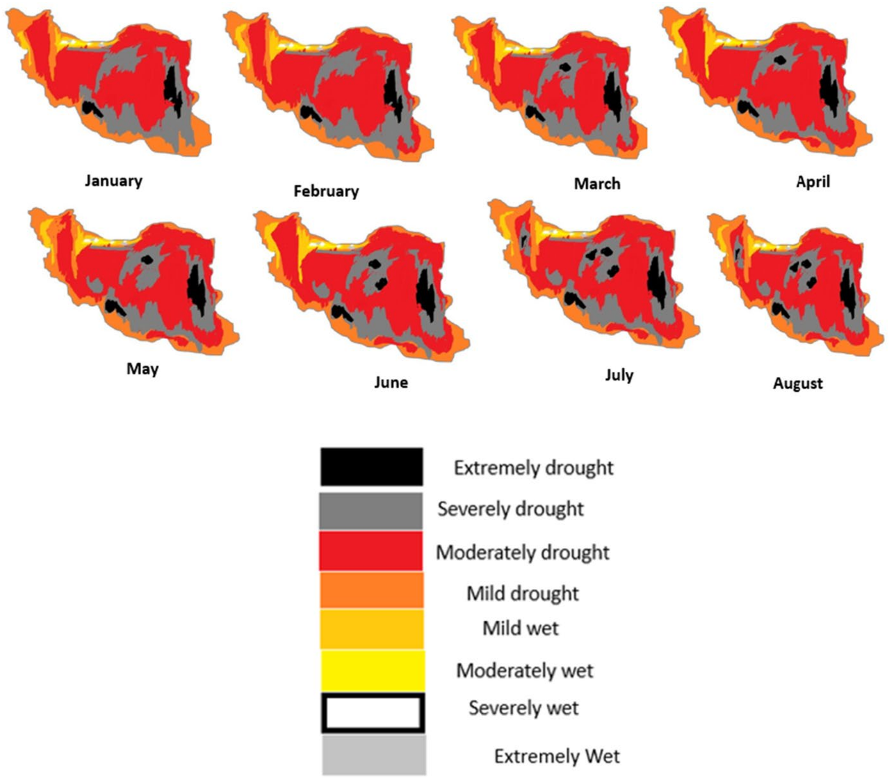

Fig. 13 The provided drought maps by the ANFIS–NPA

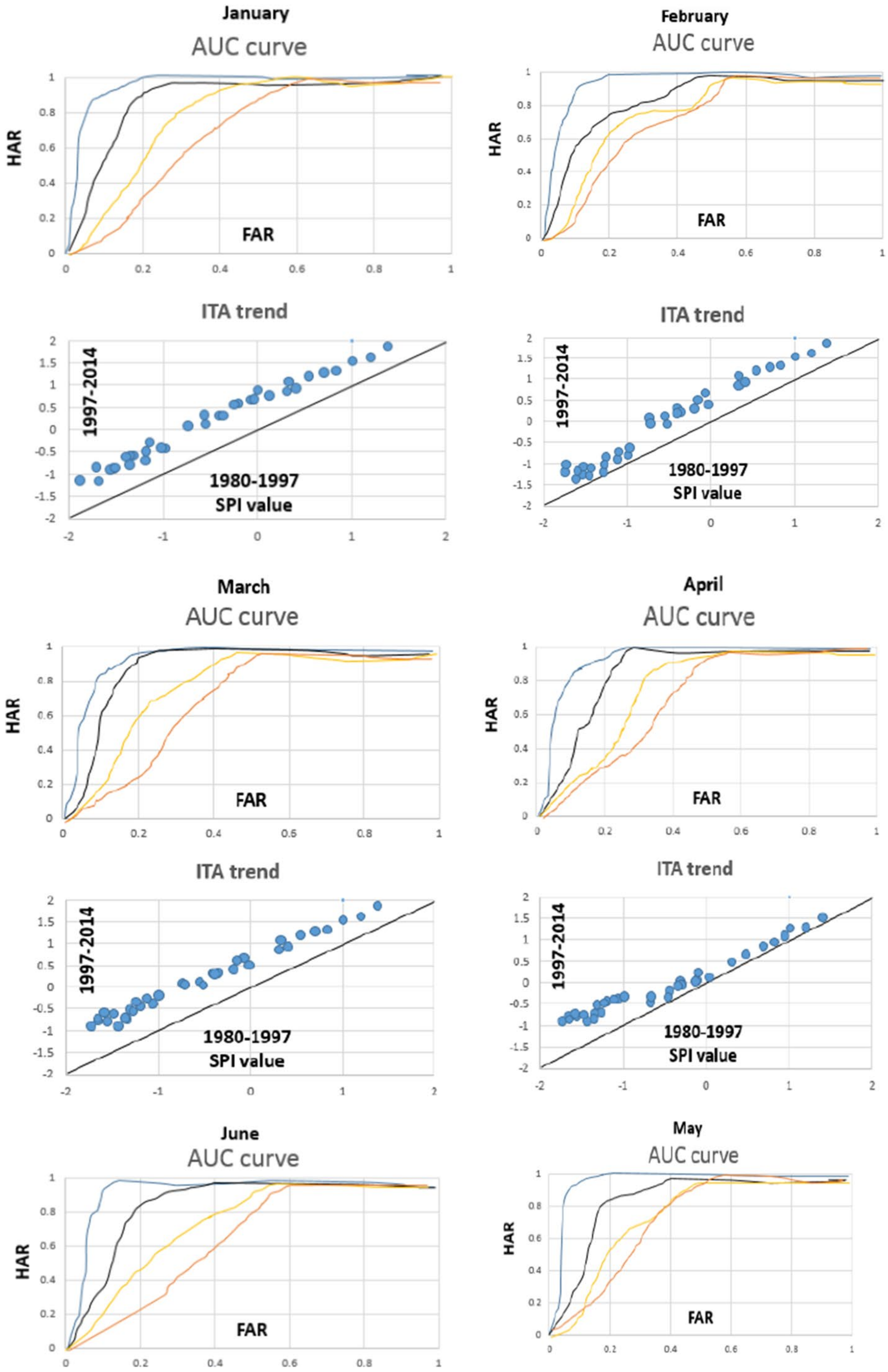

Fig. 14 The drought trend in Iran country and the AUC plot of extremely drought classification as a sample

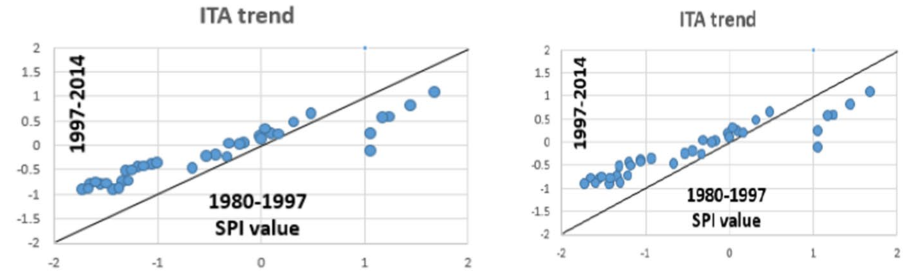

July

August

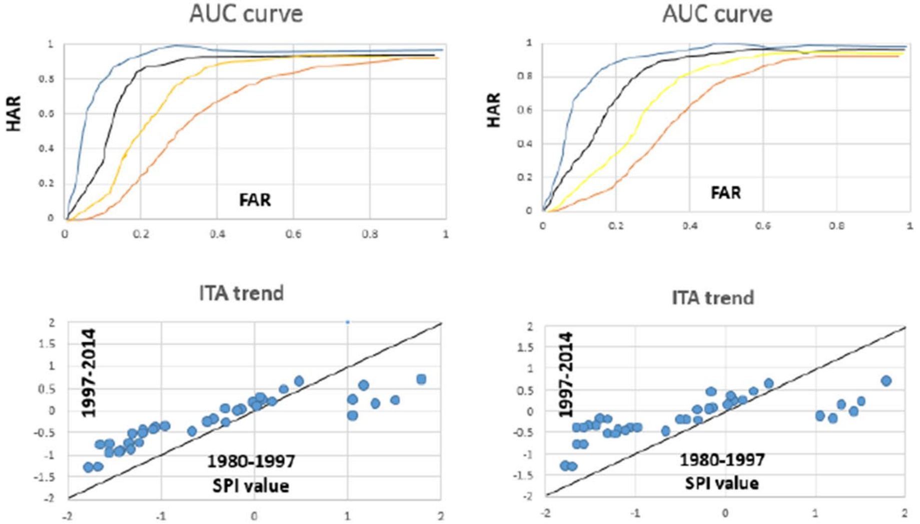

October

September

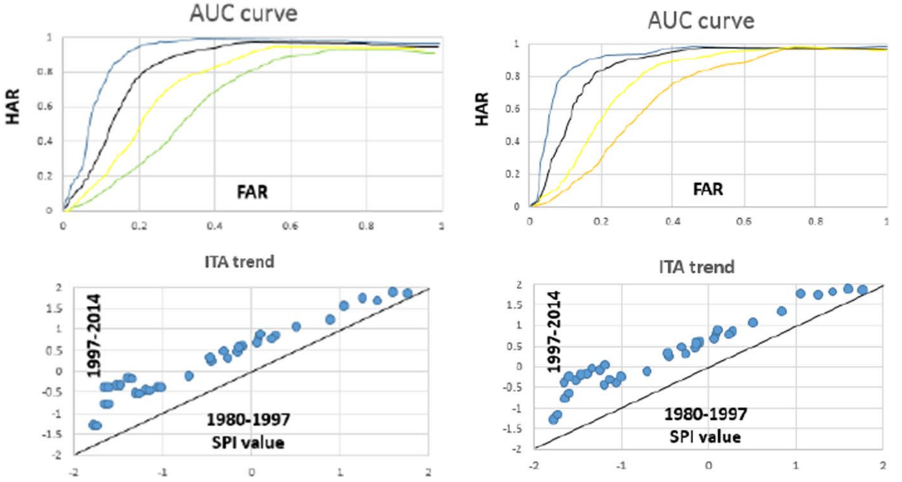

Fig. 14 (continued)

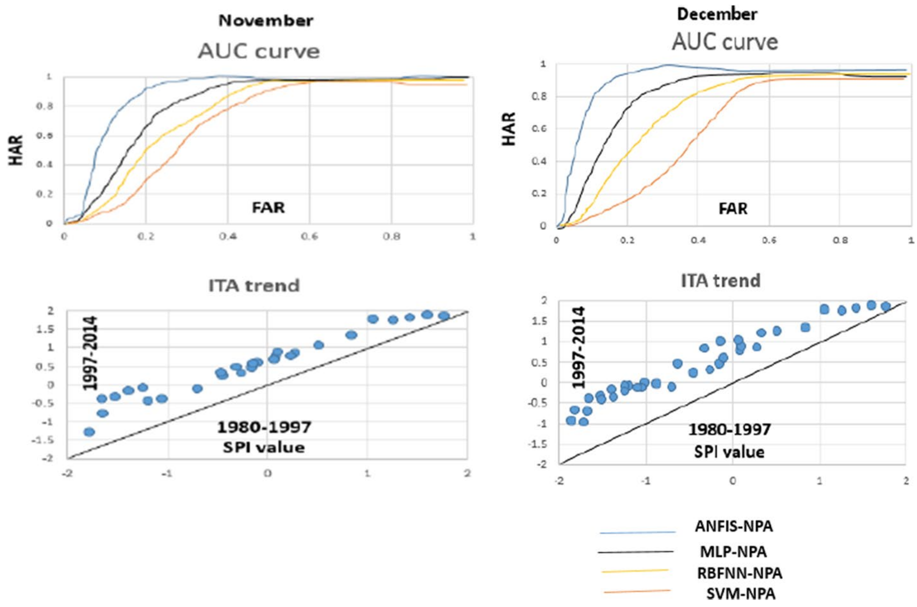

Fig. 14 (continued)

optimization algorithms is an important issue for predicting hydrological variables. The results of the large climate indices indicated that the drought intensity was significantly affected by these indices. Thus, future researches can consider these indices as inputs to the models.

5 Conclusion

Droughts are complex and are associated with multiple climate factors. Thus, it is necessary to use accurate tools for predicting droughts. In the present study, standalone and hybrid ANFIS, SVM, MLP, and RBFNN models were used for predicting the three-month SPI. Iran was selected as a case study. First, five random stations were selected for predicting droughts. The results revealed that RMSE values for the Azarbayejan station were in the range of 1.12–1.67, 1.34–1.69, 1.38–1.71, and 1.41–1.73 for the standalone and hybrid models of ANFIS, MLP, RBFNN, and SVM, respectively. The ANFIS–NPA model gave the best performance among all the models. The performance indicators of the hybrid ANFIS, SVM, MLP, and RBFNN models showed that the hybrid soft computing models gave a more reliable performance compared to the standalone MLP, RBFNN, ANFIS and SVM models. Additionally, this study used an innovative trend analysis (ITA) to identify drought trends. With regard to monthly droughts in Iran, an increasing trend was found throughout the study period in *January*. In February, the results were trendless for $SPI \leq -1$; however, the index followed an increasing trend for $SPI > -1$. The second aim of the current study was to use the wavelet coherence method to capture the complex relationship between large-scale climate signals and drought indices. There was positive statistically significant correlation between Nino3.4 and the three-month SPI with a 48–65-month signal from 1980 to 2014, and it exhibited a positive correlation with a 26–34-month signal

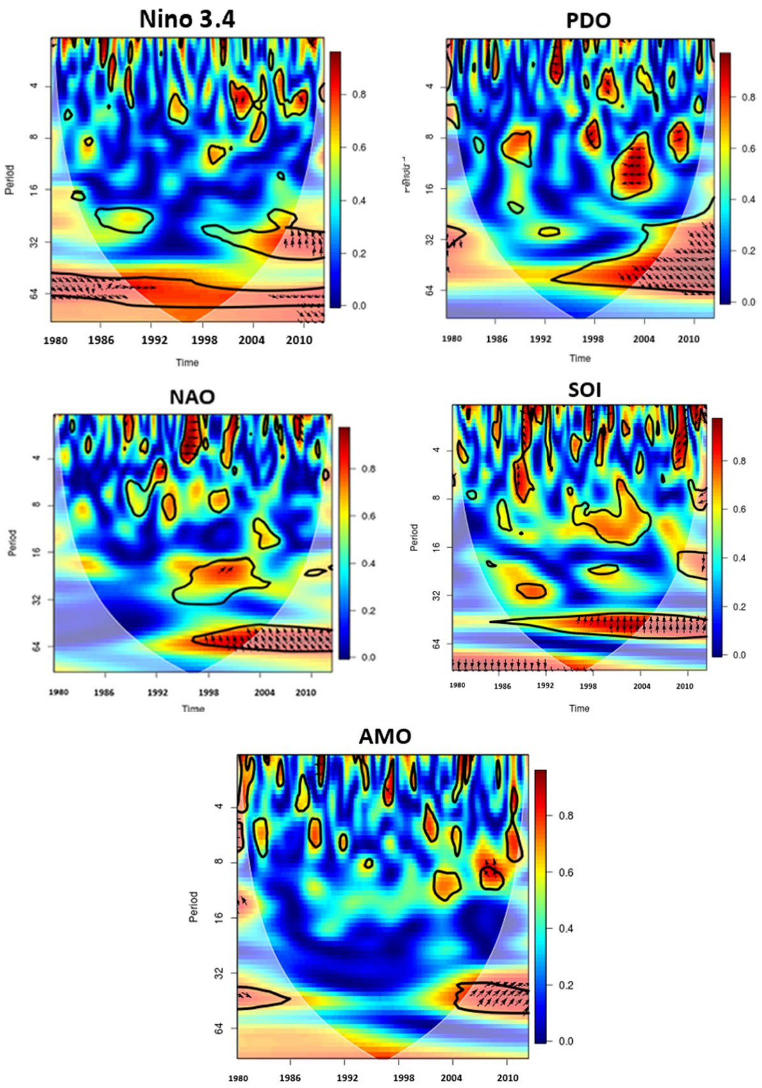

The thick contour encloses regions of greater than 95% confidence for a red-noise process

- Time is displayed on the horizontal axis, while the vertical axis shows the frequency (the lower the frequency, the higher the scale). Regions in time-frequency space where the two time series co-vary are located by the wavelet coherence.
- Warmer colors (red) represent regions with significant interrelation, while colder colors (blue) signify lower dependence between the series. Cold regions beyond the significant areas represent time and frequencies with no dependence in the series.
- An arrow in the wavelet coherence plots represents the lead/lag phase relations between the examined series. A zero phase difference means that the two time series move together on a particular scale. Arrows point to the right (left) when the time series are in phase (anti-phase).
- When the two series are in phase, it indicates that they move in the same direction, and anti-phase means that they move in the opposite direction. Arrows pointing to the right-down or left-up indicate that the first variable is leading, while arrows pointing to the right-up or left-down show that the second variable is leading.

Fig. 15 Wavelet coherence plots between large climate indexes and drought index (https://rstudio-pubs-static.s3.amazonaws.com/152496_026c3ac97f7d40e5ba0cadf757730fce.html) from 2008 to 2014. Future studies could investigate the ability of new hybrid soft computing models for predicting droughts. Thus, climate scenarios can be integrated with soft computing models for drought predictions. However, one of the limitations of this study was related to the collection of data. Also, the utilization of different climate data as the inputs to the models was an important issue. The results of this study indicated that hybrid soft computing models and wavelet coherence are appropriate tools for predicting hydrological variables.

Author contribution Conceptualization: Mohammad ehteram, Sedigheh Mohamadi, Fatemeh Panahi; Methodology: Saad Sh Sammen, Ozgur Kisi, Mohammad Ehteram; Formal analysis and investigation: Mohammad Ehteram, Amirhosein Mosavi; Writing original draft preparation: Mohammad Ehteram, Nadhir Al-Ansari, Ahmed El Shafie; Writing - review and editing: Ahmed El Shafie, Ali Najah Ahmed.

Compliance with ethical standards

Conflict of interest The authors declare that they have no conflict of interest.

References

Abd-Elazim SM, Ali ES (2016) Load frequency controller design via BAT algorithm for nonlinear interconnected power system. Int J Electr Power Energy Syst 77:166–177

Abualigah LMQ (2019) Feature selection and enhanced krill herd algorithm for text document clustering. Springer, Berlin

Aamir M, Tu S, Tolouei-Rad M, Giasin K, Vafadar A (2020) Optimization and modeling of process parameters in multi-hole simultaneous drilling using Taguchi method and fuzzy logic approach. Materials 13(3):680

Ali Ghorbani M, Kazempour R, Chau KW, Shamshirband S, Taherei Ghazvinei P (2018) Forecasting pan evaporation with an integrated artificial neural network quantum-behaved particle swarm optimization model: a case study in Talesh, Northern Iran. Eng Appl Comput Fluid Mech 12(1):724–737

Araghi A, Martinez CJ, Adamowski J, Olesen JE (2019) Associations between large-scale climate oscillations and land surface phenology in Iran. Agric For Meteorol 278:107682

Asteris Panagiotis G et al (2019) "Krill herd algorithm-based neural network in structural seismic reliability evaluation. Mech Adv Mater Struct 26(13):1146–1153

Barua S, Perera BJC, Ng AWM, Tran D (2010) Drought forecasting using an aggregated drought index and artificial neural network. J Water Clim Change 1(3):193–206

Bayissa YA, Tadesse T, Svoboda M, Wardlow B, Poulsen C, Swigart J, Van Andel SJ (2019) Developing a satellite-based combined drought indicator to monitor agricultural drought: a case study for Ethiopia. GISci Remote Sens 56(5):718–748

Borji M, Malekian A, Salajegheh A, Ghadimi M (2016) Multi-time-scale analysis of hydrological drought forecasting using support vector regression (SVR) and artificial neural networks (ANN). Arab J Geosci 9(19):725

Bozorg-Haddad O, Karimirad I, Seifollahi-Aghmiuni S, Loáiciga HA (2015) Development and application of the bat algorithm for optimizing the operation of reservoir systems. J Water Resour Plan Manag 141(8):04014097

Belayneh A, Adamowski J, Khalil B, Quilty J (2016) Coupling machine learning methods with wavelet transforms and the bootstrap and boosting ensemble approaches for drought prediction. Atmos Res 172:37–47

Bui DT, Tuan TA, Hoang ND, Thanh NQ, Nguyen DB, Van Liem N, Pradhan B (2017) Spatial prediction of rainfall-induced landslides for the Lao Cai area (Vietnam) using a hybrid intelligent approach of least squares support vector machines inference model and artificial bee colony optimization. Landslides 14(2):447–458

Chen S, Chung G, Kim BS, Kim TW (2019) Modified analogue forecasting in the hidden Markov framework for meteorological droughts. Sci China Technol Sci 62(1):151–162

Cohen JR, So FK, Hankin BL, Young JF (2019) Translating cognitive vulnerability theory into improved adolescent depression screening: A receiver operating characteristic approach. J Clin Child Adolesc Psychol 48(4):582–595

Cui Zhihua et al (2019) Optimal LEACH protocol with modified bat algorithm for big data sensing systems in Internet of Things. J Parallel Distrib Comput 132:217–229

Cheng CT, Lin JY, Sun YG, Chau K (2005) Long-term prediction of discharges in Manwan Hydropower using adaptive-network-based fuzzy inference systems models. In: International conference on natural computation. Springer, Berlin, pp 1152–1161.

Cui Z, Li F, Zhang W (2019) Bat algorithm with principal component analysis. Int J Mach Learn Cybern 10(3):603–622

Das J, Jha S, Goyal MK (2020) On the relationship of climatic and monsoon teleconnections with monthly precipitation over meteorologically homogenous regions in India: Wavelet & global coherence approaches. Atmos Res 238:104889

Deo RC, Kisi O, Singh VP (2017) Drought forecasting in eastern Australia using multivariate adaptive regression spline, least square support vector machine and M5Tree model. Atmos Res 184:149–175

Deo RC, Salcedo-Sanz S, Carro-Calvo L, Saavedra-Moreno B (2018) Drought prediction with standardized precipitation and evapotranspiration index and support vector regression models. In: Integrating disaster science and management. Elsevier, pp 151–174

Fernandez D, Gonzalez C, Mozos D, Lopez S (2019) FPGA implementation of the principal component analysis algorithm for dimensionality reduction of hyperspectral images. J Real-Time Image Proc 16(5):1395–1406

Ghorbani MA, Deo RC, Karimi V, Yaseen ZM, Terzi O (2018) Implementation of a hybrid MLP-FFA model for water level prediction of Lake Egirdir, Turkey. Stoch Env Res Risk Assess 32(6):1683–1697

Gholami A, Bonakdari H, Zaji AH, Ajeel Fenjan S, Akhtari AA (2016) Design of modified structure multilayer perceptron networks based on decision trees for the prediction of flow parameters in 90 open-channel bends. Eng Appl Comput Fluid Mech 10(1):193–208

Gibson AJ, Verdon-Kidd DC, Hancock GR, Willgoose G (2019) Catchment-scale drought: capturing the whole drought cycle using multiple indicators. Hydrol Earth Syst Sci Discuss. https://doi.org/10.5194/hess-2019-311

Hao Z, Singh VP, Xia Y (2018) Seasonal drought prediction: advances, challenges, and future prospects. Rev Geophys 56(1):108–141

Hosseini-Moghari SM, Araghinejad S, Azarnivand A (2017) Drought forecasting using data-driven methods and an evolutionary algorithm. Model Earth Syst Environ 3(4):1675–1689

Huang S, Huang Q, Leng G, Liu S (2016) A nonparametric multivariate standardized drought index for characterizing socioeconomic drought: a case study in the Heihe River Basin. J Hydrol 542:875–883

Joshi N, Gupta D, Suryavanshi S, Adamowski J, Madramootoo CA (2016) Analysis of trends and dominant periodicities in drought variables in India: a wavelet transform based approach. Atmos Res 182:200–220

Karri C, Jena U (2016) Fast vector quantization using a Bat algorithm for image compression. Eng Sci Technol Int J 19(2):769–781

Kaur A, Sood SK (2019) Artificial intelligence-based model for drought prediction and forecasting. Comput J. https://doi.org/10.1093/comjnl/bxz105

Khosravi I, Jouybari-Moghaddam Y, Sarajian MR (2017) The comparison of NN, SVR, LSSVR and ANFIS at modeling meteorological and remotely sensed drought indices over the eastern district of Isfahan Iran. Nat Hazards 87(3):1507–1522

Kisi O, Gorgij AD, Zounemat-Kermani M, Mahdavi-Meymand A, Kim S (2019) Drought forecasting using novel heuristic methods in a semi-arid environment. J Hydrol 578:124053

Le MH, Perez GC, Solomatine D, Nguyen LB (2016) Meteorological drought forecasting based on climate signals using artificial neural network–a case study in Khanhhoa Province Vietnam. Procedia Eng 154:1169–1175

Li R, Chen N, Zhang X, Zeng L, Wang X, Tang S, Niyogi D (2020a) Quantitative analysis of agricultural drought propagation process in the Yangtze River Basin by using cross wavelet analysis and spatial autocorrelation. Agric For Meteorol 280:107809

Li Q, He P, He Y, Han X, Zeng T, Lu G, Wang H (2020b) Investigation to the relation between meteorological drought and hydrological drought in the upper Shaying River Basin using wavelet analysis. Atmos Res 234:104743

Liu X, Zhu X, Zhang Q, Yang T, Pan Y, Sun P (2020) A remote sensing and artificial neural network-based integrated agricultural drought index: index development and applications. CATENA 186:104394

Lu C, Feng J, Liu W, Lin Z, Yan S (2019) Tensor robust principal component analysis with a new tensor nuclear norm. IEEE Trans Pattern Anal Mach Intell 42:925–938

McKee TB, Doesken NJ, Kleist J (1993) The relationship of drought frequency and duration to time scales. In: Proceedings of the 8th conference on applied climatology, vol 17, pp 179–183

Malik A, Kumar A, Singh RP (2019) Application of heuristic approaches for prediction of hydrological drought using multi-scalar streamflow drought index. Water Resour Manage 33(11):3985–4006

Manzano A, Clemente MA, Morata A, Luna MY, Beguería S, Vicente-Serrano SM, Martín ML (2019) Analysis of the atmospheric circulation pattern effects over SPEI drought index in Spain. Atmos Res 230:104630

Moazenzadeh R, Mohammadi B, Shamshirband S, Chau KW (2018) Coupling a firefly algorithm with support vector regression to predict evaporation in northern Iran. Eng Appl Comput Fluid Mech 12(1):584–597

Mokhtarzad M, Eskandari F, Vanjani NJ, Arabasadi A (2017) Drought forecasting by ANN, ANFIS, and SVM and comparison of the models. Environ Earth Sci 76(21):729

Mirjalili S, Gandomi AH, Mirjalili SZ, Saremi S, Faris H, Mirjalili SM (2017) Salp Swarm Algorithm: a bio-inspired optimizer for engineering design problems. Adv Eng Softw 114:163–191

Muslim TO, Ahmed AN, Malek MA et al (2020) Investigating the influence of meteorological parameters on the accuracy of sea-level prediction models in Sabah Malaysia. Sustainability 12:1193. https://doi.org/10.3390/su12031193

Najah AA, El-Shafie A, Karim OA, Jaafar O (2012) Water quality prediction model utilizing integrated wavelet-ANFIS model with cross-validation. Neural Comput Appl 21:833–841. https://doi.org/10.1007/s00521-010-0486-1

Najah Ahmed A, Binti Othman F, Abdulmohsin Afan H et al (2019) Machine learning methods for better water quality prediction. J Hydrol 578:124084. https://doi.org/10.1016/j.jhydrol.2019.124084

Nguyen V, Li Q, Nguyen L (2017) Drought forecasting using ANFIS—a case study in drought prone area of Vietnam. Paddy Water Environ 15(3):605–616

Nobre GG, Hunink JE, Baruth B, Aerts JC, Ward PJ (2019) Translating large-scale climate variability into crop production forecast in Europe. Sci Rep 9(1):1–13

Pulluri H, Kumar NG, Rao UM, Kumar MG (2019) Krill Herd Algorithm for solution of economic dispatch with valve-point loading effect. In: Applications of computing, automation and wireless systems in electrical engineering. Springer, Singapore, pp 383–392

Rahimi Y, Bihamta MR, Taleei A, Alipour H, Ingvarsson PK (2019) Applying an artificial neural network approach for drought tolerance screening among Iranian wheat landraces and cultivars grown under well-watered and rain-fed conditions. Acta Physiol Plant 41(9):156

Rahmati O, Falah F, Dayal KS, Deo RC, Mohammadi F, Biggs T, Bui DT (2020) Machine learning approaches for spatial modeling of agricultural droughts in the south-east region of Queensland Australia. Sci Total Environ 699:134230

Rezaeian-Zadeh M, Tabari H (2012) MLP-based drought forecasting in different climatic regions. Theoret Appl Climatol 109(3–4):407–414

Rezaeianzadeh M, Stein A, Cox JP (2016) Drought forecasting using Markov chain model and artificial neural networks. Water Resour Manage 30(7):2245–2259

Salih SQ, Alsewari AA (2019) A new algorithm for normal and large-scale optimization problems: nomadic people optimizer. Neural Comput Appl 32:10359–10386

Saghafian B, Haghnegahdar A, Dehghani M (2017) Effect of ENSO on annual maximum floods and volume over threshold in the southwestern region of Iran. Hydrol Sci J 62(7):1039–1049

Satgé F, Hussain Y, Xavier A, Zolá RP, Salles L, Timouk F, Bonnet MP (2019) Unraveling the impacts of droughts and agricultural intensification on the Altiplano water resources. Agric For Meteorol 279:107710

Şen Z (2012) Innovative trend analysis methodology. J Hydrol Eng 17:1042–1046. https://doi.org/10.1061/(ASCE)HE.1943-5584.0000556

Shamshirband S, Hashemi S, Salimi H, Samadianfard S, Asadi E, Shadkani S, Chau KW (2020) Predicting standardized streamflow index for hydrological drought using machine learning models. Eng Appl Comput Fluid Mech 14(1):339–350

Su L, Miao C, Duan Q, Lei X, Li H (2019) Multiple-wavelet coherence of world's large rivers with meteorological factors and ocean signals. J Geophys Res Atmos 124(9):4932–4954

Shi H, Chen J, Wang K, Niu J (2018) A new method and a new index for identifying socioeconomic drought events under climate change: a case study of the East River basin in China. Sci Total Environ 616:363–375

Tamaddun KA, Kalra A, Ahmad S (2017) Wavelet analyses of western US streamflow with ENSO and PDO. J Water Clim Change 8(1):26–39

Tortoe C, Orchard J, Beezer A, Tetteh J (2011) Application of radial basis function network with a Gaussian function of artificial neural networks in osmo-dehydration of plant materials. J Artif Intell 4(4):233–244

Tharakeshwar TK, Seetharamu KN, Prasad BD (2017) Multi-objective optimization using bat algorithm for shell and tube heat exchangers. Appl Therm Eng 110:1029–1038

Vazifehkhah S, Kahya E (2019) Hydrological and agricultural droughts assessment in a semi-arid basin: Inspecting the teleconnections of climate indices on a catchment scale. Agric Water Manag 217:413–425

Wang Y, Quan Q, Shen B (2019) Spatio-temporal variability of drought and effect of large scale climate in the source region of Yellow River. Geom Nat Hazards Risk 10(1):678–698

Wang WC, Xu L, Chau KW, Xu DM (2020) Yin-Yang firefly algorithm based on dimensionally Cauchy mutation. Expert Syst Appl 150:113216

Wu CL, Chau KW (2013) Prediction of rainfall time series using modular soft computing methods. Eng Appl Artif Intell 26(3):997–1007

Zhang Y, Yang H, Cui H, Chen Q (2019) Comparison of the ability of ARIMA, WNN and SVM models for drought forecasting in the Sanjiang Plain China. Nat Resour Res. https://doi.org/10.1007/s11053-019-09512-6

Zhao Z, Lou Y, Chen Y, Lin H, Li R, Yu G (2019) Prediction of interfacial interactions related with membrane fouling in a membrane bioreactor based on radial basis function artificial neural network (ANN). Biores Technol 282:262–268

Zhou Y, Luo Q, Xie J, Zheng H (2016) A hybrid bat algorithm with path relinking for the capacitated vehicle routing problem. In: Yang X-S, Bekdaş G, Nigdeli SM (eds) Metaheuristics and optimization in civil engineering. Springer, Cham, pp 255–276

Affiliations

Sedigheh Mohamadi[1] · Saad Sh. Sammen[2] · Fatemeh Panahi[3] · Mohammad Ehteram[4] · Ozgur Kisi[5,6] · Amir Mosavi[7,8] · Ali Najah Ahmed[9] · Ahmed El-Shafie[10,11] · Nadhir Al-Ansari[12]

[1] Department of Ecology, Institute of Science and High Technology and Environmental Sciences, Graduate University of Advanced Technology, Kerman, Iran

[2] Department of Civil Engineering, College of Engineering, University of Diyala, Baqubah, Diyala Governorate, Iraq

[3] Faculty of Natural Resources and Earth Sciences, University of Kashan, Kashan, Iran

[4] Department of Water Engineering and Hydraulic Structures, Faculty of Civil Engineering, Semnan University, Semnan, Iran

[5] Department of Civil Engineering, School of Technology, Ilia State University, 0162 Tbilisi, Georgia

[6] Institute of Research and Development, Duy Tan University, Da Nang 550000, Vietnam

[7] Environmental Quality, Atmospheric Science and Climate Change Research Group, Ton Duc Thang University, Ho Chi Minh City, Vietnam

[8] Faculty of Environment and Labour Safety, Ton Duc Thang University, Ho Chi Minh City, Vietnam

[9] Institute of Energy Infrastructure (IEI), Universiti Tenaga Nasional (UNITEN), 43000 Kajang, Selangor Darul Ehsan, Malaysia

[10] Department of Civil Engineering, Faculty of Engineering, University of Malaya (UM), 50603 Kuala Lumpur, Malaysia

[11] National Water Center (NWC), United Arab Emirates University, P.O. Box 15551, Al Ain, UAE

[12] Civil, Environmental and Natural Resources Engineering, Lulea University of Technology,
97187 Luleå, Sweden